

A Variational Quantum Algorithm for Nonlinear Finite Element Analysis of Hyperelastic Materials

Uditnarayan Kouskiya[‡], Caglar Oskay^{‡,§ *}

[‡]Department of Civil and Environmental Engineering

[§]Department of Mechanical Engineering

Vanderbilt University

Nashville, TN 37212

Abstract

This manuscript explores a variational quantum formulation for nonlinear elasticity problems arising from hyperelastic material models, targeting near-term noisy intermediate-scale quantum (NISQ) devices. The approach leverages the potential energy structure of hyperelasticity and employs a hybrid quantum–classical framework in which the energy functional is evaluated using parameterized quantum circuits and optimized through classical routines. To enable implementation on current quantum hardware, polynomial approximations of the nonlinear strain energy density are introduced, yielding a representation compatible with variational quantum algorithms. The methodology is demonstrated on a one-dimensional Neo-Hookean material model using finite element discretizations with first- and second-order shape functions and nonhomogeneous boundary conditions. Numerical experiments investigate the influence of the polynomial approximation order on the accuracy and efficiency of the proposed approach, illustrating its feasibility for near-term quantum devices.

1 Introduction

Numerical evaluation of nonlinear partial differential equations (PDEs) sits at the foundation of computational mechanics. A common approach to solving nonlinear mechanics problems is to obtain an algebraic system following discretization, which is then solved iteratively. The computational cost of the overall process grows rapidly with the system size. As demand for simulation of large, complex material and structural systems increases, such computations place significant pressure on conventional computing architectures, particularly due to performance, memory, and energy-efficiency limitations associated with the von Neumann computing architectures [1]. Quantum computing (QC) has recently emerged as an alternative computing paradigm, owing to the exponential growth of its accessible state space with the number of qubits [2, 3, 4]. In this work, we take an initial step in developing and investigating a quantum algorithm suited for near-term noisy intermediate-scale quantum (NISQ) devices, directed toward problems in nonlinear elasticity by considering a Neo-Hookean material model as a representative case.

*Corresponding author address: VU Station B#351831, 2301 Vanderbilt Place, Nashville, TN 37235. Email: caglar.oskay@vanderbilt.edu

The majority of the relevant existing QC literature focuses on the evaluation of linear ordinary differential equations (ODEs) and PDEs. A common solution approach is to construct a linear system of equations following discretization, and evaluating it using quantum linear systems algorithms (QLSAs) [5, 6]. The foundational work by Harrow et al. [7] (HHL) introduced the first QLSA, which solves sparse linear systems $Ax = b$ by encoding the right-hand side vector b as a quantum state $|b\rangle$. Using Hamiltonian simulation [8] and quantum phase estimation, the algorithm prepares a state $|x\rangle \propto A^{-1}|b\rangle$ that encodes the properties of the solution vector x . Subsequent developments produced high-precision QLSA variants based on linear combination of unitaries (LCU) [9], quantum singular value transformation (QSVT) [10], and adiabatic approaches [11]. In the context of computational mechanics, Cao et al. [12] proposed an HHL-type quantum algorithm for solving the Poisson equation using a finite-difference discretization, demonstrating polynomial speedups under sparsity and conditioning assumptions. Montanaro and Pallister [13] analyzed the application of QLSAs to finite element discretizations of elliptic boundary value problems, showing that quantum methods can provide polynomial improvements for estimating functionals of the solution. However, despite their favorable asymptotic complexity, the aforementioned approaches require deep circuits and error rates that are beyond the capabilities of the NISQ-era hardware [14].

Within the framework of near-term quantum computing, Variational Quantum Algorithms (VQAs) have emerged as a prominent and widely explored class of algorithms [15, 16]. The central idea behind VQAs is to offload the computationally intensive parts of a problem to a quantum processor that evaluates a cost function using parameterized quantum circuits encoding the quantity of interest. The circuit parameters are then iteratively updated by a classical optimizer to minimize this cost function. For example, the Variational Quantum Linear Solver (VQLS) [17] is designed to compute solutions to linear systems, and was employed by Arora et al. [18] to compute solutions to finite element method (FEM)-based steady state heat equation with various mesh configurations. Similarly, Rao et al. [19] employed VQLS for plane strain elasticity problems.

The extension of quantum algorithms to nonlinear problems in mechanics remains challenging due to the inherently linear structure of quantum operations. Consequently, many approaches approximate nonlinear response through linear embeddings. For example, Endo and Takahashi [20] employed Carleman linearization to reformulate nonlinear differential equations as higher dimensional linear systems amenable to quantum algorithms. Similarly, Xu et al. [21] proposed a quantum nonlinear solver based on the asymptotic numerical method, demonstrating its application to a beam buckling problem by expanding the nonlinear system into a power series and reducing it to a sequence of linear systems. These approaches assume access to fault-tolerant quantum hardware. Lubasch et al. [22] introduced a novel VQA framework for nonlinear PDEs with polynomial nonlinearities by devising quantum nonlinear processing units and demonstrated the efficacy of this approach on Burgers and nonlinear Schrödinger equations. Samra et al. [23] recently extended this approach to solve a broader class of nonlinear PDEs.

The idea expressed in Lubasch et al. [22] (and subsequent related works) rely on a least-square functional as the cost function. Sato et al. [24] proposed a VQA to solve the Poisson equation by formulating the corresponding Dirichlet energy as a cost function parameterized by a quantum circuit. The energy terms were evaluated using a quantum oracle, and the circuit parameters were optimized classically to minimize the cost, thereby encoding the solution. Similarly, Over and Bengoechea et al. [25, 26], also derived a variational form for the advection–diffusion equation in the time-discrete setting and minimized it within a VQA framework.

This manuscript presents a VQA-based approach for nonlinear elasticity problems arising from hyperelastic material models under certain assumptions. The proposed framework exploits the fact that, for hyperelastic materials, the stress is derived from a strain energy density function, thereby enabling a variational formulation of elasticity in terms of a total potential energy functional

[27]. We introduce polynomial approximation strategies for representing nonlinear terms in the strain energy density function in a manner compatible with current VQA implementations. The resulting approximated potential energy functional is constructed to integrate naturally within a variational quantum framework. The proposed methodology is demonstrated on a simplified one-dimensional Neo-Hookean material based problem. Two distinct approximation strategies are developed and implemented in accordance with contemporary VQA capabilities. The displacement field is discretized using first- and second-order finite element shape functions, and the formulation accommodates nonhomogeneous boundary conditions. The influence of higher-order polynomial approximations on the efficiency and accuracy of the VQA implementation is evaluated.

The remainder of this manuscript is organized as follows. Section 2 presents the overview of the proposed approach. The governing equations for a general multidimensional problem are first introduced and then restricted to the one-dimensional setting. The resulting potential energy is then embedded into a VQA framework, concluding with an outline of the overall VQA procedure. Section 3 applies the scheme to a Neo-Hookean material model, introducing the energy functional, deriving a quantum-computing-compatible approximation, and constructing its discretized form using finite element shape functions and Gaussian quadrature. Section 4 provides the details of the quantum implementation. The basic quantum circuits used as building blocks, the state preparation procedure for encoding real-valued vectors, and the evaluation of the individual terms in the cost function based on specifically designed quantum circuits are described. In Section 5, we analyze the gate and time complexity of the proposed approach. Section 6 presents numerical results demonstrating the performance of the VQA for different polynomial approximation orders and for first- and second-order finite element discretizations. Section 7 summarizes the main findings and outlines directions for future research.

2 Overview of the Proposed Approach

In this section, we outline the proposed VQA-based approach for nonlinear elasticity problems involving hyperelastic materials. We begin by formulating the governing equations and deriving a simplified model suitable for analysis. The VQA framework requires a cost function to optimize, which we construct from the system’s potential energy. To evaluate this energy on a quantum computer, the displacement field (represented by its discretized values) must be encoded as a quantum state. This motivates the introduction of a quantum representation of real-valued vectors. Finally, we integrate these components to establish a complete framework for approximating the solution to the underlying elasticity problem.

2.1 Mathematical model

The nonlinear elastostatic boundary-value problem in the reference configuration $\Omega_0 \subset \mathbb{R}^3$ ($\mathbf{X} = (X, Y, Z)$) is given by

$$\nabla_{\mathbf{X}} \cdot \mathbf{P}(\mathbf{F}(\mathbf{X})) + \mathbf{B}(\mathbf{X}) = \mathbf{0} \quad \text{for } \mathbf{X} \in \Omega_0, \quad (1a)$$

$$\mathbf{F} = \nabla_{\mathbf{X}} \varphi = \mathbf{I} + \nabla_{\mathbf{X}} \mathbf{u}(\mathbf{X}) \quad (1b)$$

$$\mathbf{u}(\mathbf{X}) = \bar{\mathbf{u}}(\mathbf{X}) \quad \text{for } \mathbf{X} \in \Gamma_D, \quad (1c)$$

$$\mathbf{P} \cdot \mathbf{N} = \bar{\mathbf{P}}(\mathbf{X}) \quad \text{for } \mathbf{X} \in \Gamma_N, \quad (1d)$$

where \mathbf{P} is the first Piola-Kirchhoff stress tensor, φ the deformation map, $\mathbf{u} = (u, v, w)$ the displacement, \mathbf{F} the deformation gradient and \mathbf{B} the body force per unit reference volume. \mathbf{N} is the outward unit normal at the reference domain boundaries, and $\bar{\mathbf{u}}$ and $\bar{\mathbf{P}}$ are prescribed displacements

and tractions, respectively. The Dirichlet and Neumann boundaries are denoted as $\Gamma_D \subset \partial\Omega_0$ and $\Gamma_N \subset \partial\Omega_0$, respectively, such that $\Gamma_D \cup \Gamma_N = \partial\Omega_0$ and $\Gamma_D \cap \Gamma_N = \emptyset$. For hyperelastic materials, the stress follows from a strain energy density $W(\mathbf{F})$ via $\mathbf{P} = \partial W / \partial \mathbf{F}$. For such materials, it is a classical result that there exists a potential energy functional

$$\mathcal{E}[\mathbf{u}] = \int_{\Omega_0} W(\mathbf{F}) \, dV - \int_{\Omega_0} \mathbf{B} \cdot \mathbf{u} \, dV - \int_{\Gamma_N} \bar{\mathbf{P}} \cdot \mathbf{u} \, dA, \quad (2)$$

up to a constant that depends on the applied traction and the body force. The critical points of \mathcal{E} satisfy the weak form of the governing equations (1). The number and nature of the critical points (i.e., minima vs. saddle points) of the potential energy functional depend on the properties of W [27].

We consider a one-dimensional reduction of the above three-dimensional theory. Specifically, we assume that the reference configuration is a prismatic body of constant cross-sectional area A , such that

$$\Omega_0 = (0, L) \times A, \quad (3)$$

where $A \subset \mathbb{R}^2$. We further assume that all fields depend only on the axial coordinate X , and that the deformation is uniaxial along the X -direction. The lateral surface $(0, L) \times \partial A$ is assumed to be traction-free, while the remainder of the boundary conditions are prescribed on the end faces at $X = 0$ and $X = L$.

Under these assumptions, the deformation gradient reduces to

$$\mathbf{F}(\mathbf{X}) = \text{diag}(\lambda(X), 1, 1), \quad (4)$$

where

$$\lambda(X) = 1 + u'(X) \quad (5)$$

represents the principal stretch in the axial direction and $(\cdot)' \equiv d(\cdot)/dX$. Physical admissibility requires

$$J(\mathbf{X}) = \det \mathbf{F}(\mathbf{X}) = \lambda(X) > 0, \quad \forall X \in (0, L) \quad (6)$$

Since all fields are uniform over the cross-section, volume and surface integrals factor into the cross-sectional area A , multiplied by one-dimensional integrals over $(0, L)$. For simplicity, and without loss of generality, we work per unit reference cross-sectional area (i.e., $|A| = 1$), so that the three-dimensional formulation reduces to a one-dimensional problem on the interval

$$\Omega_0 = (0, L), \quad \partial\Omega_0 = \{0, L\}. \quad (7)$$

The Dirichlet and Neumann boundaries therefore correspond to subsets of the endpoints.

Consequently, we consider the one-dimensional reduction of the potential energy functional: (2):

$$\mathcal{E}[u] := \int_{\Omega_0} W(\lambda) \, dX - \int_{\Omega_0} B(X) u(X) \, dX - \sum_{X \in \Gamma_N} \bar{P} u(X), \quad (8)$$

where B represents the body force, \bar{P} the prescribed axial traction and W is a function of λ only. The stationary point of the above functional yields the following weak form:

For $u = \bar{u}$ on Γ_D , find u such that

$$\int_{\Omega_0} P(\lambda) v' \, dX = \int_{\Omega_0} B v \, dX + \sum_{X \in \Gamma_N} \bar{P} v, \quad \forall v \in H^1(\Omega_0); \quad v = 0 \text{ on } \Gamma_D \quad (9)$$

where $P(\lambda) = \partial W / \partial \lambda$.

Under sufficient smoothness assumptions on the displacement field, the weak form is equivalent to the strong form (equilibrium equation) in the axial direction, given by:

$$\frac{d}{dX}(P(\lambda(X))) + B(X) = 0 \quad \text{in } \Omega_0, \quad (10)$$

subject to the boundary conditions

$$u = \bar{u} \quad \text{on } \Gamma_D, \quad P = \bar{P} \quad \text{on } \Gamma_N. \quad (11)$$

2.2 Quantum representation of real vectors

Unlike classical computing where information is represented using *bits* that take values of 0 or 1, quantum computing uses *qubits*—quantum two-level systems—that can exist in a superposition of the 0 and 1 states. The computational basis states for a single qubit are denoted as $|0\rangle$ and $|1\rangle$. For a register of n qubits, the corresponding Hilbert space has dimension $N_q = 2^n$. The computational basis states are denoted as

$$\{|\text{bin}(k)\rangle \mid k = 0, 1, \dots, 2^n - 1\}, \quad (12)$$

where k is the integer label of the basis state, and its binary representation specifies the state of each qubit. For example, in a three-qubit system, $|\text{bin}(5)\rangle$ corresponds to the quantum state $|101\rangle$, which indicates that the first and third qubits are in state $|1\rangle$, while the second qubit is in state $|0\rangle$. In what follows, we use $|k\rangle$ instead of $|\text{bin}(k)\rangle$ for simplicity, unless otherwise stated.

Any real vector $\mathbf{p} \in \mathbb{R}^{N_q}$ (complex vectors are admissible, but we restrict our attention to real valued vectors), is encoded as a quantum state $|\hat{p}\rangle$ (or simply \hat{p} when no confusion arises), such that:

$$\sum_{i=0}^{N_q-1} p_i \mathbf{e}_i = \mathbf{p} = \|\mathbf{p}\| |\hat{p}\rangle = \|\mathbf{p}\| \sum_{k=0}^{N_q-1} \hat{p}_k |k\rangle, \quad (13)$$

noting that the quantum state $|\hat{p}\rangle$ is normalized.

Any quantum state $|\hat{p}\rangle$ is prepared on a quantum computer using a parameterized quantum circuit, or *Ansatz* circuit, represented by a unitary operator $\widehat{V}(\boldsymbol{\lambda}_p)$, where

$$\boldsymbol{\lambda}_p = (\lambda_{p_1}, \lambda_{p_2}, \dots, \lambda_{p_m}); \quad \lambda_{p_i} \in [0, 2\pi], \quad (14)$$

is the set of ansatz parameters (each element corresponds to a rotation angle applied to a qubit). When applied to the initial basis state $|0\rangle$, it yields:

$$|\hat{p}\rangle = \widehat{V}(\boldsymbol{\lambda}_p) |0\rangle. \quad (15)$$

The ansatz defines a parameterized trial space of quantum states, whose structure determines its ability to approximate the target state. Different ansatz constructions employ specific arrangements of single-qubit rotation gates and two-qubit entangling gates, which govern the expressiveness of the resulting state space. In this work, we adopt the ansatz proposed by Sim et al. [28], shown in Fig. 1. Other ansatz choices with sufficient expressiveness could be used in its place without loss of generality. Ansatz parameters along with the scaling parameter $\lambda_{p_0} := \|\mathbf{p}\|$, are collectively referred to as the *control parameters* and generate the vector \mathbf{p} based on (13).

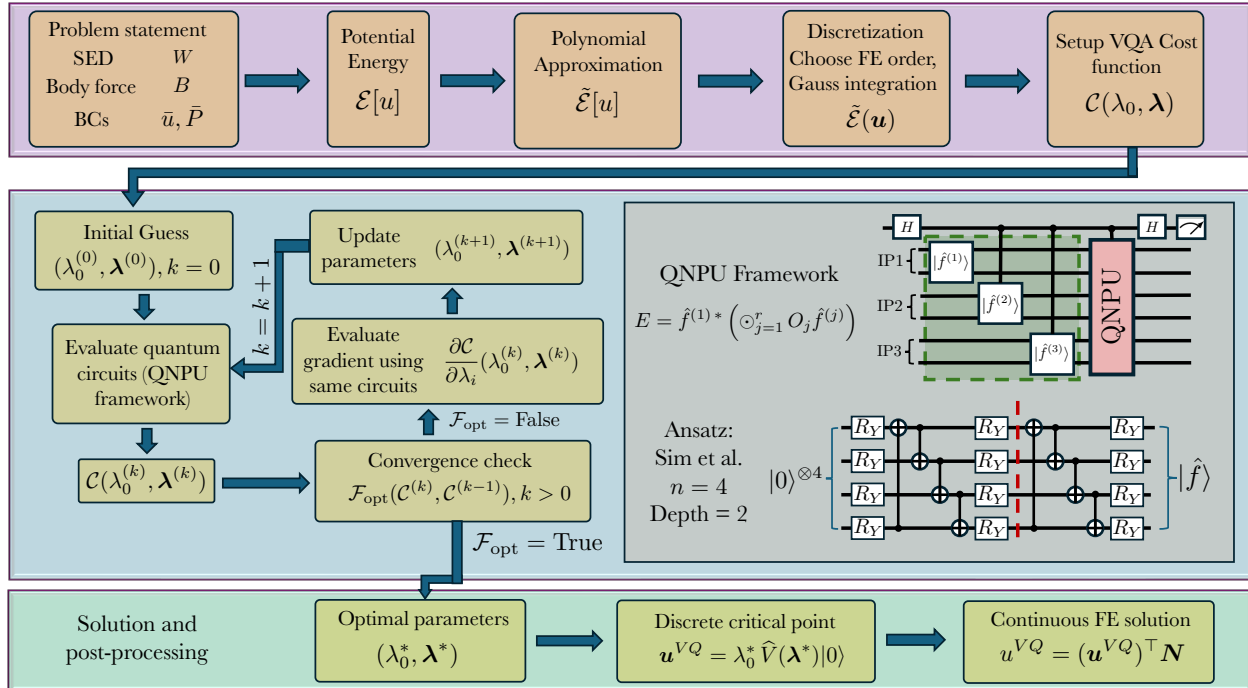


Figure 1: VQA Framework.

2.3 Variational Quantum Algorithm

The overall structure of the proposed VQA framework is depicted in Fig. 1. The workflow consists of two main phases: a setup phase (purple) and an optimization phase (blue). At its core, the method represents the unknown displacement field through a set of tunable control parameters, which are iteratively adjusted to approximate the solution.

In the setup phase, the elasticity problem is specified via its strain energy density, which defines the corresponding potential energy functional. This functional is considered for evaluation using quantum circuits, with the control parameters serving as circuit input. Instead of assembling element-wise contributions, the quantum approach directly estimates global or macroscopic quantities (expectation values) of interest. In particular, expectation values from a small set of circuits, are combined classically to estimate the total potential energy of the system.

A key challenge, however, arises from the inherently linear nature of quantum operations, which makes the direct implementation of nonlinear transformations involved in the potential energy difficult. Existing methods for nonlinear transformations can be resource-intensive [29]. Instead, we propose low-degree polynomial approximations of arbitrary nonlinearities, which can be implemented using relatively shallow quantum circuits known as Quantum Nonlinear Processing Units (QNPUs) as developed in [22] and are more suitable for near-term NISQ devices.

Accordingly, any nonlinearity $\mathcal{G}(u')$ in the functional (8) is approximated as

$$\mathcal{G}(u') \approx \sum_{i=0}^{N_{tn}} c_i (u')^i, \quad (16)$$

where N_{tn} denotes the truncation order, yielding an approximated functional denoted by $\tilde{\mathcal{E}}$. Let \mathbf{u} denote the discrete vector representing the field u and the functional $\tilde{\mathcal{E}}[u]$ be written as a function

$\tilde{\mathcal{E}}(\mathbf{u})$. Accordingly, we define the VQA cost function as follows:

$$\mathcal{C}(\lambda_0, \boldsymbol{\lambda}) := \tilde{\mathcal{E}}(\mathbf{u}(\lambda_0, \boldsymbol{\lambda})). \quad (17)$$

Each term in $\tilde{\mathcal{E}}$ is further decomposed into components suitable for quantum evaluation. The corresponding circuits, with the control parameters as inputs, are executed independently, and their expectation values are combined classically to estimate the cost function.

The second phase is concerned with a classical optimization process to iteratively update the control parameters using a gradient-based optimizer, aimed at searching for a critical point of the approximate potential energy (via cost function). The gradients $(\partial\mathcal{C}/\partial\lambda_i)$ computed via finite differences use the same circuits as that of the cost function. A cost function value based stopping criteria \mathcal{F}_{opt} terminates the optimization. The optimal parameters $(\lambda_0^*, \boldsymbol{\lambda}^*)$ identify the discrete profile

$$\mathbf{u}^* = \lambda_0^* \widehat{V}(\boldsymbol{\lambda}^*)|0\rangle, \quad (18)$$

which corresponds to a critical point of $\tilde{\mathcal{E}}$ and is therefore taken as the solution.

3 Application to Neo-Hookean Material Model

For the current work, we focus on a Neo-Hookean hyperelastic model, for which the strain energy density function is given as:

$$W(\mathbf{F}) = \frac{\mu}{2} \left(\text{tr}(\mathbf{F}^\top \mathbf{F}) - \text{ndim} \right) - \mu \ln J + \frac{\Lambda}{2} (\ln J)^2, \quad (19)$$

where μ and Λ are Lamé's parameters and ndim represents the number of dimensions. We invoke (4) and set $\Lambda = 0$. The strain energy density function reduces to a function of the principal stretch λ only:

$$W(\lambda) = \frac{\mu}{2} (\lambda^2 - 1 - 2 \ln \lambda) \quad (20)$$

The equilibrium equation (10) reduces to:

$$\frac{d}{dX} \left(\mu \left(1 + u' - (1 + u')^{-1} \right) \right) + B = 0 \quad \text{in } \Omega_0 \quad (21)$$

where

$$P = \mu \left(\lambda - \frac{1}{\lambda} \right) \quad \text{and} \quad \lambda = 1 + u', \quad (22)$$

were used. We employ the following boundary conditions:

$$u(0) = \bar{u}, \quad (23a)$$

$$P(L) = \bar{P}, \quad (23b)$$

where the boundary condition $P(L) = \bar{P}$ implies

$$1 + u'(L) - (1 + u'(L))^{-1} = \frac{\bar{P}}{\mu}. \quad (24)$$

The corresponding potential energy functional \mathcal{E} can be written explicitly in u :

$$\mathcal{E}[u] = \int_{\Omega_0} \left(\mu \left(u' + \frac{1}{2} (u')^2 - \ln(1 + u') \right) - B u \right) dX - \bar{P} u(L), \quad (25)$$

where $u'(X) > -1 \forall X \in \Omega_0$. In this case, it can be shown that for admissible displacements satisfying $u'(X) > -1$, the second variation of the energy functional is strictly positive. Consequently, the functional is strictly convex on the admissible set, implying the existence of a unique minimizer. This minimizer coincides with the unique weak solution of the governing equation and, under sufficient regularity, satisfies the strong form (21).

3.1 QC Compatible Approximation of the Energy

Evaluating (25) within a quantum framework would require us to deal with the logarithmic nonlinear term. As an illustrative example, the logarithmic term appearing in (25) may be approximated using a Taylor series expansion,

$$\ln(1 + u') \approx u' - \frac{1}{2} (u')^2 + \frac{1}{3} (u')^3 - \dots + \frac{(-1)^{n+1}}{n} (u')^n; \quad (26a)$$

$$-1 < u' < 1 \quad (26b)$$

Substituting this approximation into the original energy functional (25) yields the truncated polynomial energy

$$\tilde{\mathcal{E}}[u] = \mathcal{E}_B[u] + \mathcal{E}_2[u] + \sum_{i \geq 3} \mathcal{E}_i[u] - \bar{P} u(L), \quad (27)$$

where the individual contributions are given by

$$\mathcal{E}_B[u] = - \int_{\Omega_0} B u \, dX, \quad (28a)$$

$$\mathcal{E}_2[u] = \int_{\Omega_0} \mu (u')^2 \, dX, \quad (28b)$$

$$\mathcal{E}_i[u] = \frac{(-1)^i}{i} \int_{\Omega_0} \mu (u')^i \, dX. \quad (28c)$$

For regimes in which $u' > 1$, a more suitable representation of the logarithmic term may be obtained using the inverse hyperbolic tangent (IHT) expansion [30],

$$\ln(1 + u') \approx 2 \left(\frac{u'}{u'+2} + \frac{1}{3} \left(\frac{u'}{u'+2} \right)^3 + \dots + \frac{1}{2n-1} \left(\frac{u'}{u'+2} \right)^{2n-1} \right). \quad (29)$$

To incorporate this expansion while maintaining a polynomial energy representation, we introduce an auxiliary variable y and define the augmented energy functional

$$\tilde{\mathcal{E}}[u, y] = \int_{\Omega_0} \left[\mu \left(u' + \frac{1}{2} (u')^2 - 2 \left(y + \frac{1}{3} y^3 \right) \right) - B u + \frac{\mathcal{P}}{2} (u' y + 2y - u')^2 \right] dX - \bar{P} u(L), \quad (30)$$

where $\mathcal{P} \gg 1$ is the penalty parameter enforcing the constraint

$$y \approx u' / (u' + 2) \quad (31)$$

during minimization (the expansion has been truncated after two terms). The above functional is amenable to implementation within a quantum framework which is explained in the following subsections. The resulting variational problem is to determine

$$(u^*, y^*) = \arg \min_{u, y} \tilde{\mathcal{E}}[u, y], \quad \text{subject to } u(0) = \bar{u}. \quad (32)$$

Fig. 2 compares the accuracy of the two types of expansions.

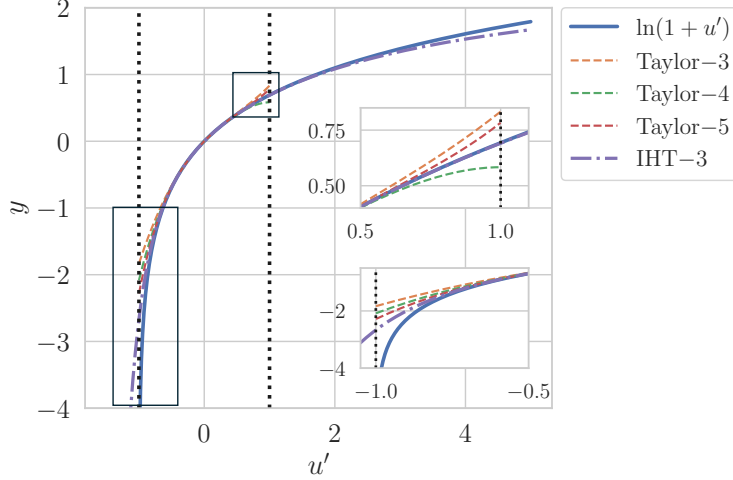


Figure 2: Approximations to the logarithmic nonlinearity. The Taylor series expansion is valid only within $-1 < u' < 1$. y represents different approximations.

3.2 Finite Element Discretization

We employ a Ritz-type approximation in which the solution field is expressed as a finite expansion in terms of trial (basis) functions [31]. In the present work, these trial functions coincide with standard finite-element shape functions. This section presents the discrete integral structure for various terms in (25), arising from the polynomial order of basis functions. This structure is then exploited to design the quantum circuits.

Let the domain Ω_0 be discretized into finite elements with $N_q + 1$ nodal points such that $N_q = 2^n$ where n represents the number of main qubits (one node is reserved as Dirichlet boundary condition). The number of elements depends on the polynomial order of the shape functions employed; for instance, N_q linear elements or $N_q/2$ quadratic elements.

The finite element approximation of an arbitrary field f is given by

$$\tilde{f}(X) := \sum_{i=0}^{N_q} f_i N_i(X) = \mathbf{f}^\top \mathbf{N}, \quad (33)$$

where $N_i(X)$ denotes the Lagrange shape function associated with node i , and f_i is the corresponding nodal value.

Within an element e , the FE approximation can be written in local form as

$$\tilde{f}(X(\xi)) = \sum_{i=0}^{N_{en}-1} f_{i_e} \hat{N}_i(\xi), \quad (34)$$

where i indexes the N_{en} local nodes of element e and i_e represents the global node number associated with the local node i . In this work,

$$i_e = \begin{cases} i + e & \text{for 1st order shape functions;} \\ i + 2e & \text{for 2nd order shape functions.} \end{cases} \quad (35)$$

The derivative of \tilde{f} with respect to the physical coordinate X , restricted to element e , is

$$\tilde{f}'(X) = \sum_{i=0}^{N_{en}-1} f_{i_e} N'_{i_e}(X), \quad (36)$$

where the derivatives of the shape functions follow from the chain rule:

$$N'_{i_e}(X) = \widehat{N}'_i(\xi(X)) (J_e(\xi(X)))^{-1}, \quad J_e(\xi) = \frac{dX}{d\xi}. \quad (37)$$

Here $J_e(\xi)$ is the Jacobian of the mapping from the reference element to physical element e , and $\xi(X)$ denotes the inverse mapping within element e .

The integral of \tilde{f} over the element Ω_e is approximated via Gaussian quadrature as

$$\int_{\Omega_e} \tilde{f}(X) dX \approx \sum_{g=0}^{N_{gp}-1} w^{(g)} J_e^{(g)} \tilde{f}(X^{(g)}), \quad (38)$$

where N_{gp} is the number of Gauss points in the element, $w^{(g)}$ is the quadrature weight at Gauss point g , $J_e^{(g)}$ is the Jacobian evaluated at $\xi^{(g)}$ for element e , and $X^{(g)} = X_e(\xi^{(g)})$ is the corresponding physical coordinate in Ω_e .

3.2.1 First order FE shape functions

For first order FE shape functions and two-point Gauss quadrature, let

$$\alpha_i^{(I,g)} = \widehat{N}_i(\xi^{(g)}) \quad \text{and} \quad \alpha_i^{(II,g)} = \widehat{N}'_i(\xi^{(g)}). \quad (39)$$

Accordingly, $\tilde{f}(X^{(g)})$ reduces to:

$$\begin{aligned} \tilde{f}(X^{(0)}) &= f_{0_e} \alpha_0^{(I,0)} + f_{1_e} \alpha_1^{(I,0)} = \alpha f_{0_e} + (1 - \alpha) f_{1_e}; \\ \tilde{f}(X^{(1)}) &= f_{0_e} \alpha_0^{(I,1)} + f_{1_e} \alpha_1^{(I,1)} = (1 - \alpha) f_{0_e} + \alpha f_{1_e}; \\ \alpha &= \frac{\sqrt{3} + 1}{2\sqrt{3}}. \end{aligned} \quad (40)$$

Similarly, the derivative of \tilde{f} within any element e and at Gauss point g can be approximated as:

$$\tilde{f}'(X^{(g)}) = \sum_{i=0}^1 f_{i_e} N'_{i_e}(X^{(g)}) = \sum_{i=0}^1 \frac{2 f_{i_e}}{h_e} \alpha_i^{(II,g)} = \frac{f_{1_e} - f_{0_e}}{h_e}, \quad (41)$$

where h_e denotes the length of element e . Using (40) and (41), each of the terms in (28) can be approximated via the following element-wise quadrature evaluations:

$$\tilde{\mathcal{E}}_2(\mathbf{u}) = \mu \int_{\Omega_0} (\tilde{u}')^2 dX = \mu \sum_{e=0}^{N_q-1} h_e \left(\frac{u_{1_e} - u_{0_e}}{h_e} \right)^2; \quad (42a)$$

$$\tilde{\mathcal{E}}_i(\mathbf{u}) = \mu \int_{\Omega_0} \frac{(-1)^i}{i} (\tilde{u}')^i dX = \mu \left(\frac{(-1)^i}{i} \right) \sum_{e=0}^{N_q-1} h_e \left(\frac{u_{1_e} - u_{0_e}}{h_e} \right)^i; \quad (42b)$$

$$\tilde{\mathcal{E}}_B(\mathbf{u}) = - \int_{\Omega_0} B \tilde{u} dX = \sum_{e=0}^{N_q-1} \sum_{g=0}^1 \frac{h_e}{2} B(X_e^{(g)}) \tilde{u}(X_e^{(g)}). \quad (42c)$$

A similar discrete decomposition for the functional (30) is presented in Appendix B.

3.2.2 Second Order Shape Functions

For simplicity, the central node within an element is placed at the center the element: $X_{1_e} = (X_{0_e} + X_{2_e})/2$. As a consequence, the value of Jacobian over the length of the domain becomes a constant: $J_e(\xi) = h_e/2$. For second order FE shape functions and any Gauss point g , we introduce

$$\beta_i^{(I,g)} := \widehat{N}_i(\xi^{(g)}) \quad \text{and} \quad \beta_i^{(II,g)} = \widehat{N}'_i(\xi^{(g)}). \quad (43)$$

The value of the function \tilde{f} is expressed as

$$\tilde{f}(X^{(g)}) = \sum_{i=0}^2 f_{i_e} \beta_i^{(I,g)}. \quad (44)$$

where the values of $\beta_i^{(I,g)}$ is established in a straightforward way. Similarly, the derivative is approximated as:

$$\tilde{f}'(X^{(g)}) = \sum_{i=0}^2 f_{i_e} N'_{i_e}(X^{(g)}) = 2 \sum_{i=0}^2 \frac{f_{i_e} \beta_i^{(II,g)}}{h_e}. \quad (45)$$

For a two point Gauss quadrature (for simplicity) and $N_{el} = N_q/2$ number of elements, we obtain the following:

$$\tilde{\mathcal{E}}_2(\mathbf{u}) = \mu \sum_{e=0}^{N_{el}-1} \sum_{g=0}^1 \left(\frac{2}{h_e}\right) \left(\sum_{j=0}^2 u_{j_e} \beta_j^{(II,g)}\right)^2, \quad (46a)$$

$$\tilde{\mathcal{E}}_i(\mathbf{u}) = \mu \left(\frac{(-1)^i}{i}\right) \sum_{e=0}^{N_{el}-1} \sum_{g=0}^1 \left(\frac{2}{h_e}\right)^{i-1} \left(\sum_{j=0}^2 u_{j_e} \beta_j^{(II,g)}\right)^i, \quad (46b)$$

$$\tilde{\mathcal{E}}_B(\mathbf{u}) = - \sum_{e=0}^{N_{el}-1} \sum_{g=0}^1 \frac{h_e}{2} \left(\sum_{j=0}^2 u_{j_e} \beta_j^{(I,g)}\right) B(X_e^{(g)}). \quad (46c)$$

4 Implementation of the Cost Function

This section focuses on the construction of the approximate discretized energy functional $\tilde{\mathcal{E}}$ using quantum circuits. We begin by introducing the circuits that serve as the fundamental building blocks for evaluating the cost function. We then describe the state-preparation procedure used to encode real-valued vectors as quantum states. Finally, we show how these components are combined to evaluate the discrete integrals using quantum circuits, thereby enabling the computation of the cost function.

4.1 Algorithmic Primitives

All quantum circuits employed in this work are constructed within a common framework built upon the idea of a Quantum Nonlinear Processing Unit (QNPU) [22]. The template circuit representing a framework for the calculations, referred to as the QNPU framework, is shown in Fig. 1. Circuits with different QNPU blocks enable the evaluation of scalar quantities of the form

$$E = \hat{f}^{(1)\top} \left(\odot_{j=1}^r O_j \hat{f}^{(j)} \right), \quad (47)$$

where O_j denotes a linear operator acting on the input quantum state $\hat{f}^{(j)}$, and \odot represents the element-wise (Hadamard) product across the vectors $\{O_j \hat{f}^{(j)}\}_{j=1}^r$. The input states $\hat{f}^{(j)}$ are prepared on separate quantum registers (input ports), which are subsequently processed by the QNPU block through entangling operations. Following this processing stage, E is measured using an ancilla qubit, without requiring full state tomography. In what follows, we refer to this ancilla as the *Hadamard ancilla*, to distinguish it from other types of ancilla qubits. In particular,

$$E = \mathbb{P}(0) - \mathbb{P}(1), \quad (48)$$

where $\mathbb{P}(0)$ and $\mathbb{P}(1)$ are the probabilities of measuring $|0\rangle$ and $|1\rangle$ on the Hadamard ancilla, respectively.

4.1.1 Inner Product via QNPU

Let $\mathbf{p}, \mathbf{q} \in \mathbb{R}^{N_q}$ be real vectors parameterized by control parameters $(\lambda_{p_0}, \boldsymbol{\lambda}_p)$ and $(\theta_{q_0}, \boldsymbol{\theta}_q)$, respectively, for a fixed ansatz:

$$\mathbf{p} = \|\mathbf{p}\| |\hat{p}\rangle = \lambda_{p_0} \hat{V}(\boldsymbol{\lambda}_p) |0\rangle, \quad \mathbf{q} = \|\mathbf{q}\| |\hat{q}\rangle = \theta_{q_0} \hat{V}(\boldsymbol{\theta}_q) |0\rangle. \quad (49)$$

The inner product between \mathbf{p} and \mathbf{q} is given by

$$\mathbf{p}^\top \mathbf{q} = \|\mathbf{p}\| \|\mathbf{q}\| \langle \hat{p} | \hat{q} \rangle = \lambda_{p_0} \theta_{q_0} \langle 0 | \hat{V}^\dagger(\boldsymbol{\lambda}_p) \hat{V}(\boldsymbol{\theta}_q) | 0 \rangle. \quad (50)$$

Comparing (50) with (47) (up to the scaling factor and setting $r = 1$), we identify $|\hat{f}^{(1)}\rangle = |0\rangle$, which, being the initial computational basis state, does not require state preparation. The corresponding operator is given by

$$O_1 = \hat{V}^\dagger(\boldsymbol{\lambda}_p) \hat{V}(\boldsymbol{\theta}_q), \quad (51)$$

which is implemented within the QNPU framework, as illustrated in Fig. 3a. This circuit requires $n + 1$ qubits.

4.1.2 Diagonal Operators

To evaluate quantities involving element-wise (Hadamard) products of more than two quantum state vectors, we introduce diagonal operators. As an illustrative example, consider the quantity

$$\mathbf{p}^\top (\mathbf{q} \odot \mathbf{p}), \quad (52)$$

which can be expressed as

$$\mathbf{p}^\top (\mathbf{q} \odot \mathbf{p}) = \|\mathbf{p}\|^2 \|\mathbf{q}\| \sum_{i=0}^{N_q-1} \hat{p}_i^2 \hat{q}_i = \lambda_{p_0}^2 \lambda_{q_0} \langle \hat{p} | D_{\hat{q}} | \hat{p} \rangle, \quad (53)$$

where $D_{\hat{q}}$ is a diagonal operator defined by

$$(D_{\hat{q}})_{ii} = \hat{q}_i. \quad (54)$$

For simplicity, we will often use

$$(D_{\mathbf{q}})_{ii} = \|\mathbf{q}\| \hat{q}_i. \quad (55)$$

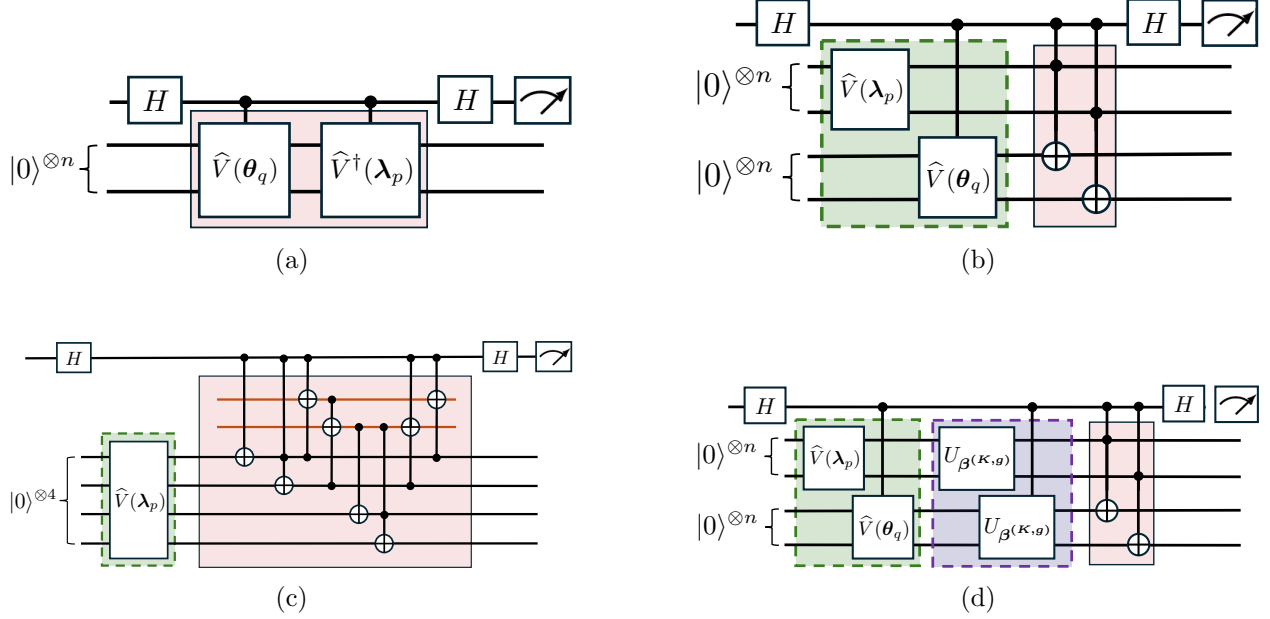


Figure 3: Primitive circuits to evaluate (a) $\langle \hat{p} | \hat{q} \rangle$, (b) $\langle \hat{p} | D_{\hat{q}} | \hat{p} \rangle$, (c) $\langle \hat{p} | \hat{A} | \hat{p} \rangle$, and (d) $\|\ell_p\|^2 \|\ell_q\| \langle \hat{p} | D_{\hat{q}} | \hat{p} \rangle$; The green, red, and purple regions denote the input, QNPU, and block-encoding phases, respectively. In (c), the two red qubit registers correspond to the ancillas required by the Adder circuit. In (d), ancillas associated with the block-encoding components are omitted for clarity.

The action of $D_{\hat{q}}$ on the state $|\hat{p}\rangle$ is given by

$$D_{\hat{q}}|\hat{p}\rangle = \sum_{i=0}^{N_q-1} \hat{q}_i \hat{p}_i |i\rangle, \quad (56)$$

which corresponds to elementwise (Hadamard) scaling of the amplitudes of $|\hat{p}\rangle$ by those of $|\hat{q}\rangle$.

The circuit diagram to evaluate (53), up to the scaling factor is shown in Fig. 3b. Comparing (53) with (47), we identify $|\hat{f}^{(1)}\rangle = |\hat{p}\rangle$, prepared independently of the Hadamard ancilla in input port 1, while $|\hat{f}^{(2)}\rangle$ is prepared in input port 2 under Hadamard ancilla control. These inputs are combined within the QNPU through the action of the diagonal operator. The expectation value obtained from measuring the Hadamard ancilla (cf. (48)) yields the quantity in (52), up to a normalization factor. Additional input ports may be appended and entangled with input port 1 in the same manner as input port 2, yielding expressions of the form

$$\mathbf{p}^\top (\mathbf{q}_1 \odot \mathbf{q}_2 \odot \cdots \odot \mathbf{q}_{N_t} \odot \mathbf{p}), \quad (57)$$

where $\mathbf{q}_i \in \mathbb{R}^{N_q}$, $i = \{1, 2, \dots, N_t\}$, represent additional input vectors. The corresponding circuit for evaluating the above expression employs $N_t + 1$ input ports and a total of $n(N_t + 1) + 1$ qubits.

4.1.3 Adder Circuit

The adder circuit \hat{A} acts on a state $|\hat{p}\rangle$ as a cyclic shift operator, producing $\hat{A}|\hat{p}\rangle = \sum_{k=0}^{N_q-1} \hat{p}_{k+1} |k\rangle$, where the index shift is understood modulo N_q [32, 22]. This operation can be implemented using quantum circuits that typically require $n - 2$ ancillas. Alternatively, an ancilla-free implementation

based on the Quantum Fourier Transform (QFT) can be used, albeit at the cost of increased circuit depth [33].

When embedded within the QNPU framework (see Fig. 3c), a total of $2n - 1$ qubits are required. This circuit enables the evaluation of inner products involving shifted vectors. In particular,

$$\mathbf{p}^\top(\widehat{A}\mathbf{p}) = \|\mathbf{p}\|^2 \langle \hat{p} | \widehat{A} | \hat{p} \rangle = \lambda_{p_0}^2 \langle \hat{p} | \widehat{A} | \hat{p} \rangle. \quad (58)$$

In circuit constructions combining multiple primitive operations, several adder circuits may be required. Although the ancillas used in each adder operation evolve during computation, they are ultimately uncomputed and restored to the $|0\rangle$ state. Consequently, the same ancilla register can be reused across successive controlled or uncontrolled adder circuits, thereby reducing the overall ancilla overhead.

4.1.4 Block Encoding within QNPU

Quantum circuits implement only unitary transformations, whereas many operators of interest are generally non-unitary. To realize such operators within a quantum circuit framework, we use *block encoding*, where a non-unitary matrix is embedded into a larger unitary operator acting on an extended Hilbert space.

For an operator $\mathbf{A} \in \mathbb{C}^{2^s \times 2^s}$, an exact block encoding consists of a unitary $\widehat{U}_{\mathbf{A}}$ acting on the system together with ancillary qubits such that

$$(\langle 0^{\otimes a} | \otimes I) \widehat{U}_{\mathbf{A}} (|0^{\otimes a}\rangle \otimes I) = \frac{\mathbf{A}}{\alpha}, \quad (59)$$

where $\alpha > 0$ is a normalization factor such that the scaled operator \mathbf{A}/α can be embedded within a unitary operator and a is the number of ancilla qubits.

Equivalently, when the ancilla register is initialized in the state $|0\rangle^{\otimes a}$,

$$\widehat{U}_{\mathbf{A}} (|0\rangle^{\otimes a} \otimes |\psi\rangle) = \frac{1}{\alpha} |0\rangle^{\otimes a} \otimes (\mathbf{A}|\psi\rangle) + |\Phi^\perp\rangle, \quad (60)$$

where $|\Phi^\perp\rangle$ has no support on ancilla state $|0\rangle^{\otimes a}$. Thus, postselecting the ancilla register onto the state $|0\rangle^{\otimes a}$ produces a quantum state proportional to $\mathbf{A}|\psi\rangle$, where the corresponding proportionality factor $\|\mathbf{A}|\psi\rangle\|$ is determined by the success probability of the postselection measurement.

For notational simplicity, ancilla registers and postselection operations will be omitted whenever implicit. Accordingly, we adopt the notation

$$U_{\mathbf{A}}|\psi\rangle \equiv \|\mathbf{A}|\psi\rangle\| \left(\frac{\mathbf{A}|\psi\rangle}{\|\mathbf{A}|\psi\rangle\|} \right) \quad (61)$$

to denote the effective non-unitary action of \mathbf{A} on $|\psi\rangle$ realized through the block encoding $\widehat{U}_{\mathbf{A}}$, where the bracketed term corresponds to the normalized quantum state obtained on the system registers following postselection.

In this work, we follow the construction in [34] to implement block encodings of non-unitary sparse circulant matrices. In particular, we use (39) and (43) to define the matrices $\boldsymbol{\alpha}^{(\mathbf{K},g)}, \boldsymbol{\beta}^{(\mathbf{K},g)} \in \mathbb{R}^{N_q \times N_q}$, $\mathbf{K} = \{I, II\}$, such that

$$\left(\boldsymbol{\alpha}^{(\mathbf{K},g)} \right)_{ij} = \begin{cases} \alpha_0^{(\mathbf{K},g)}, & j \equiv i \pmod{N_q}, \\ \alpha_1^{(\mathbf{K},g)}, & j \equiv i + 1 \pmod{N_q}, \quad i, j = 1, \dots, N_q, \\ 0, & \text{otherwise;} \end{cases} \quad (62)$$

and

$$\left(\beta^{(\mathbf{K},g)}\right)_{ij} = \begin{cases} \beta_0^{(K,g)}, & j \equiv i \pmod{N_q}, \\ \beta_1^{(K,g)}, & j \equiv i + 1 \pmod{N_q}, \\ \beta_2^{(K,g)}, & j \equiv i + 2 \pmod{N_q}, \\ 0, & \text{otherwise;} \end{cases} \quad i, j = 1, \dots, N_q. \quad (63)$$

The block encodings of $\alpha^{(\mathbf{K},g)}$ and $\beta^{(\mathbf{K},g)}$ require $2n$ and $2n + 1$ qubits, respectively, where n denotes the number of qubits in the main register. Each block-encoding circuit incorporates one or more adder circuits, allowing the associated $n - 2$ adder ancilla qubits to be shared and reused within and across block encodings. In addition, the block encodings of $\alpha^{(\mathbf{K},g)}$ and $\beta^{(\mathbf{K},g)}$ require 2 and 3 dedicated ancilla qubits, respectively, for postselection measurements. These ancillas cannot be reused once measured.

Embedding these block-encoded operators within the QNPU framework enables the evaluation of more complex expressions. For example, let $\mathbf{m} \in \mathbb{R}^{N_q}$ such that

$$\beta^{(\mathbf{K},g)}\mathbf{m} = \|\mathbf{m}\| U_{\beta^{(\mathbf{K},g)}}|\hat{m}\rangle = \|\mathbf{m}\|\ell_m^{(K,g)} = \|\mathbf{m}\| \left\| \ell_m^{(K,g)} \right\| \left| \hat{\ell}_m^{(K,g)} \right\rangle. \quad (64)$$

Then, using (53) and (61),

$$\left(\beta^{(\mathbf{K},g)}\mathbf{p}\right)^\top \left(\left(\beta^{(\mathbf{K},g)}\mathbf{q}\right) \odot \left(\beta^{(\mathbf{K},g)}\mathbf{p}\right) \right) = \|\mathbf{p}\|^2 \|\mathbf{q}\| \left\langle \hat{p} \left| U_{\beta^{(\mathbf{K},g)}} D_{\ell_q^{(K,g)}} U_{\beta^{(\mathbf{K},g)}} \right| \hat{p} \right\rangle, \quad (65)$$

where the bracketed quantity on the right-hand side can be evaluated using the circuit in Fig. 3d. The corresponding implementation requires a total of $3n + 5$ qubits. Of these, $2n$ qubits correspond to the input registers, $n - 2$ ancillas are used for adder operations, and one ancilla serves as the Hadamard ancilla. The remaining six ancillas (three per block encoding) are associated with the block encoding circuits and require post-measurement.

4.2 State preparation

The proposed algorithm employs a number of predefined auxiliary vectors, such as body-force fields or element-length information. This data, represented using non-normalized vectors in \mathbb{R}^{N_q} , must be incorporated into the quantum framework so that the computed solution reflects the prescribed. The quantum state $|\hat{f}\rangle$ of vector \mathbf{f} is then encoded into the relevant quantum circuit through a *state preparation* stage. In this work, we employ the same ansatz \hat{V} circuit used to represent the input state to also prepare the state $|\hat{f}\rangle$, where the required ansatz parameters are determined through an optimization procedure. Specifically, we solve

$$(\lambda_{f_0}, \boldsymbol{\lambda}_f) = \arg \min_{\lambda_0, \boldsymbol{\lambda}} \mathcal{C}_f(\lambda_0, \boldsymbol{\lambda}), \quad \text{where} \quad \mathcal{C}_f(\lambda_0, \boldsymbol{\lambda}) := \left\| \mathbf{f} - \lambda_0 \hat{V}(\boldsymbol{\lambda})|0\rangle \right\| \quad (66)$$

The tolerance for the optimization in the current work (i.e., examples below) is set to $\mathcal{C}_f \leq 10^{-5}$. In practice, reconstructing a complete amplitude vector requires tomography-like measurements, the complexity of which scales exponentially with the number of qubits, making this infeasible for large systems [35, 36]. For quantum states corresponding to simple functional forms, such as sparse vectors or amplitudes given by low-degree polynomial or piecewise-polynomial functions, existing analytic or structured state preparation techniques may be adequate [37, 38].

4.3 Evaluating discrete integrals

The discrete integrals in Section 3.2 are computed as summations over all elements, where each element involves specific interpolant-based manipulations (e.g., evaluating fields at Gauss points via interpolation of elemental Degrees of Freedom, DoFs) followed by possible nonlinear arithmetic (e.g. raising this result by a polynomial power). While these operations are performed locally in the classical finite element framework, quantum circuits act globally on the field through unitary transformations. Consequently, the local arithmetic structure must be extended to align with the global and unitary nature of the QC framework, ensuring that the classical computations can be performed in the quantum setting. To achieve this, we present two approaches: (1) a direct-expansion approach, and (2) a block-encoding based approach.

In the examples considered in this work, the mesh contains one more node than the Hilbert-space dimension $N_q = 2^n$ associated with an n -qubit register. This extra node enforces the Dirichlet boundary condition within the classical part of the computation, while the remaining degrees of freedom are encoded in the quantum state vector. For a left Dirichlet boundary condition, the global DoF vector \mathbf{u} is partitioned as

$$\mathbf{u} = (\bar{u}, \mathbf{v}), \quad \mathbf{v} = (v_0, v_1, \dots, v_{N_q-1}) = (u_1, u_2, \dots, u_{N_q}), \quad (67)$$

and $u_0 = \bar{u}$. The vector of internal displacements \mathbf{v} is parameterized using:

$$\mathbf{v} = \lambda_0 \widehat{V}(\boldsymbol{\lambda})|0\rangle. \quad (68)$$

Analogously, the quantum-encoded vector for a right Dirichlet boundary specification becomes

$$\mathbf{v} = (u_0, u_1, \dots, u_{N_q-1}). \quad (69)$$

Application of Dirichlet boundary conditions at both ends follows in a straightforward fashion:

$$\mathbf{u} = (\bar{u}_0, \mathbf{v}, \bar{u}_{N_q+1}), \quad \mathbf{v} = (u_1, u_2, \dots, u_{N_q}), \quad (70)$$

The analyses below focuses on left Dirichlet condition and a traction boundary condition on the right; however, the other two configurations discussed above can be implemented based on the same ideas presented below.

4.3.1 Direct-expansion based method

Considering (27), with the element-wise quadrature evaluations given in (42), we now present the quantum realization of each term:

The *quadratic term* (42a) is rewritten as

$$E_2 = \mu \sum_{e=0}^{N_q-1} h_e \left(\frac{u_{1e} - u_{0e}}{h_e} \right)^2 = \mu \left(\frac{\bar{u}^2}{h_0} + T_1 + T_2 + T_3 \right) \quad (71)$$

where

$$T_1 = -\frac{2\bar{u}}{h_0} v_0, \quad T_2 = \sum_{i=0}^{N_q-2} v_i^2 \left(\frac{1}{h_i} + \frac{1}{h_{i+1}} \right) + \frac{v_{N_q-1}^2}{h_{N_q-1}}, \quad T_3 = \sum_{i=0}^{N_q-2} \frac{2v_i v_{i+1}}{h_{i+1}}. \quad (72)$$

Defining

$$\mathbf{m}^{(1)} := \|\mathbf{m}^{(1)}\| |\hat{\mathbf{m}}^{(1)}\rangle = [1, 0, 0, \dots, 0], \quad (73)$$

and since \bar{u} is the prescribed Dirichlet boundary value at the left end of the domain, the term T_1 is evaluated as

$$T_1 = -2 \frac{\bar{u} \lambda_0}{h_0} \langle \hat{v} | \hat{m}^{(1)} \rangle, \quad (74)$$

where $\|\mathbf{m}^{(1)}\| = 1$, and the inner-product circuit described in Section 4.1.1 is utilized.

Similarly, T_2 can be written as

$$T_2 = \lambda_0^2 \|\mathbf{m}^{(2)}\| \langle \hat{v} | D_{\hat{m}^{(2)}} | \hat{v} \rangle, \quad (75)$$

with

$$m_i^{(2)} = \begin{cases} \frac{1}{h_i} + \frac{1}{h_{i+1}}, & i = 0, \dots, N_q - 2, \\ \frac{1}{h_{N_q-1}}, & i = N_q - 1. \end{cases} \quad (76)$$

The circuit described in Section 4.1.2 is used to evaluate this expression.

Finally, the cross term T_3 is evaluated as

$$T_3 = 2 \lambda_0^2 \|\mathbf{m}^{(3)}\| \langle \hat{v} | D_{\hat{m}^{(3)}} \hat{A}^\dagger | \hat{v} \rangle, \quad (77)$$

where

$$m_i^{(3)} = \begin{cases} \frac{1}{h_{i+1}}, & i = 0, \dots, N_q - 2, \\ 0, & i = N_q - 1. \end{cases} \quad (78)$$

This term involves a diagonal operator followed by an inverse adder circuit implemented within the QNPU block. The control parameters corresponding to $\mathbf{m}^{(\cdot)}$ are obtained using the state-preparation method described in Section 4.2.

The *cubic term* (42b) is expressed as

$$E_3 = -\frac{\mu}{3} \sum_{e=0}^{N_q-1} h_e \left(\frac{u_{1e} - u_{0e}}{h_e} \right)^3 = -\frac{\mu}{3} \left(\frac{\bar{u}^3}{h_0^2} + T_1 + T_1' + T_2 + T_3 \right), \quad (79)$$

where, using (73)

$$T_1 = -\frac{3\bar{u}^2}{h_0^2} \langle \hat{v} | \hat{m}^{(1)} \rangle, \quad T_1' = \frac{3\bar{u}}{h_0^2} \langle \hat{v} | \hat{m}^{(1)} \rangle^2, \quad (80a)$$

$$T_2 = \sum_{i=0}^{N_q-2} v_i^3 \left(\frac{1}{h_i^2} + \frac{1}{h_{i+1}^2} \right) + \frac{v_{N_q-1}^3}{h_{N_q-1}^2}, \quad T_3 = \sum_{i=0}^{N_q-2} \frac{3}{h_{i+1}^2} (v_i^2 v_{i+1} - v_i v_{i+1}^2). \quad (80b)$$

After some algebra, the latter two terms take the forms

$$T_2 = \lambda_0^3 \|\mathbf{m}^{(4)}\| \langle \hat{v} | D_{\hat{m}^{(4)}} D_{\hat{v}} | \hat{v} \rangle, \quad (81)$$

$$T_3 = 3 \lambda_0^3 \|\mathbf{m}^{(5)}\| \langle \hat{v} | D_{\hat{m}^{(5)}} D_{\hat{v}} \hat{A} | \hat{v} \rangle - 3 \lambda_0^3 \|\mathbf{m}^{(6)}\| \langle \hat{v} | D_{\hat{m}^{(6)}} D_{\hat{v}} \hat{A}^\dagger | \hat{v} \rangle, \quad (82)$$

where

$$m_i^{(4)} = \begin{cases} \frac{1}{h_i^2} + \frac{1}{h_{i+1}^2}, & i = 0, \dots, N_q - 2, \\ \frac{1}{h_{N_q-1}^2}, & i = N_q - 1, \end{cases} \quad (83)$$

and

$$m_i^{(5)} = \begin{cases} \frac{1}{h_{i-1}^2}, & i = 1, \dots, N_q - 1, \\ 0, & i = 0, \end{cases} \quad m_i^{(6)} = \begin{cases} \frac{1}{h_{i+1}^2}, & i = 0, \dots, N_q - 2, \\ 0, & i = N_q - 1. \end{cases} \quad (84)$$

Higher-order terms can be derived analogously and are omitted here for brevity. The *body force term* (42c) is expressed as

$$\tilde{\mathcal{E}}_B(\mathbf{u}) = b_0 \bar{u} + \sum_{i=0}^{N_q-1} b_{i+1} v_i, \quad (85)$$

where the coefficients b_i are given by

$$b_i = \sum_{e=0}^{N_q-1} \sum_{g=0}^1 \frac{h_e}{2} B(X_e^{(g)}) N_i(X_e^{(g)}), \quad (86)$$

where $N_i(X_e^{(g)}) = 0$ for elements not connected to node i . Introducing the vector of interior force coefficients

$$\mathbf{b} := (b_1, b_2, \dots, b_{N_q}) = \|\mathbf{b}\| |\hat{\mathbf{b}}\rangle, \quad (87)$$

and recalling that $u_0 = \bar{u}$ is prescribed, we obtain

$$\tilde{\mathcal{E}}_B(\mathbf{u}) = b_0 \bar{u} + \lambda_0 \|\mathbf{b}\| \langle \hat{\mathbf{b}} | \hat{\mathbf{v}} \rangle, \quad (88)$$

where the quantum state

$$|\hat{\mathbf{b}}\rangle = \hat{V}(\boldsymbol{\gamma})|0\rangle \quad (89)$$

is prepared using the state-preparation procedure described in Section 4.2.

The boundary contribution from (27) is given by

$$\bar{P} u(L) = \bar{P} \langle \hat{\mathbf{v}} | \hat{\mathbf{m}}^{(-1)} \rangle, \quad (90)$$

where

$$\mathbf{m}^{(-1)} := \|\mathbf{m}^{(-1)}\| |\hat{\mathbf{m}}^{(-1)}\rangle = [0, 0, \dots, 0, 1]. \quad (91)$$

The expressions corresponding to the penalty-based formulation for the IHT expansion based approximation of \mathcal{E} (cf. Appendix B) is derived analogously.

In the above derivations, all expressions—such as Gauss-point interpolations and their powers—are explicitly expanded in terms of the global degree-of-freedom vector. This motivates the term *direct-expansion* scheme. However, as the polynomial order or the order of the shape functions increases, the number of required quantum circuits grows rapidly. An alternative approach is to employ block encodings.

4.3.2 A Block-encoding-based method

In this approach, the interpolation of nodal data to Gauss points, being a linear and generally non-unitary operation, is implemented via a block encoding of the interpolation matrix, as described in Section 4.1.4. We demonstrate this approach for the second-order finite-element discretization of the energy functional presented in Section 3.2.2. Consider (46) with a two-point Gauss quadrature

scheme and a Dirichlet boundary condition at the left boundary. Rewriting (46b) by separating the contribution of the first element:

$$\tilde{\mathcal{E}}_k(\mathbf{u}) = \mu \left(\frac{(-1)^k}{k} \right) \sum_{g=0}^1 \left[\left(\frac{2}{h_0} \right)^{k-1} \left(\sum_{j=0}^2 u_{j_0} \beta_j^{(II,g)} \right)^k + \sum_{e=1}^{N_q/2-1} \left(\frac{2}{h_e} \right)^{k-1} \left(\sum_{j=0}^2 u_{j_e} \beta_j^{(II,g)} \right)^k \right]. \quad (92)$$

The contribution from the left boundary element can be constructed by finding the values of u_1 and u_2 (or equivalently v_0 and v_1) by considering their dot products, with appropriately prepared basis state vectors as considered in (73).

To compute the (bulk) contribution of internal elements (i.e., the second term on the right hand side of (92)), consider the circulant coefficient matrix $\beta^{(II,g)}$ as defined in (63) and $\ell_v^{(II,g)}$ using (64). Define $\mathbf{m}^{(7)} \in \mathbb{R}^{N_q}$ such that

$$m_i^{(7)} = \begin{cases} \left(\frac{2}{h_{\frac{i+1}{2}}} \right)^{k-1}, & i = 1, 3, \dots, N_q - 3, \\ 0, & \text{otherwise.} \end{cases} \quad (93)$$

Not all components of $\ell_v^{(II,g)}$ carry physically relevant information (e.g., those with $i = 0, 2, \dots$). The structure of $\mathbf{m}^{(7)}$ automatically suppresses these non-physical contributions. Following (65), the bulk contribution is then written as

$$\sum_{e=1}^{N_q/2-1} \left(\frac{2}{h_e} \right)^{k-1} \left(\sum_{j=0}^2 u_{j_e} \beta_j^{(II,g)} \right)^k = \lambda_0^k \langle \hat{v} | U_{\beta^{(II,g)}} D_{\ell_v^{(II,g)}}^{k-2} D_{\mathbf{m}^{(7)}} U_{\beta^{(II,g)}} | \hat{v} \rangle \quad (94)$$

where the Hadamard product is applied $k - 1$ times. The quadratic term (46a) can be evaluated analogously.

To evaluate the *body force* term (46c), we define

$$m_i^{(8,g)} = \begin{cases} \frac{1}{2} h_{\frac{i+1}{2}} B(X_i^{(g)}), & i = 1, 3, \dots, N_q - 3, \\ 0, & \text{otherwise.} \end{cases} \quad (95)$$

Then, using (63) and (64), the bulk contribution becomes

$$\sum_{e=1}^{N_q/2-1} \frac{h_e}{2} \left(\sum_{j=0}^2 u_{j_e} \beta_j^{(I,g)} \right) B(X_e^{(g)}) = \lambda_0 \|\mathbf{m}^{(8,g)}\| \langle \hat{m}^{(8,g)} | U_{\beta^{(I,g)}} | \hat{v} \rangle. \quad (96)$$

The contribution of the first element to the body force term is obtained by substituting the values of u_1 and u_2 , determined in the treatment of (46b), into (46c) and evaluating the resulting expression (contribution from first element only) classically.

5 Complexity

The complexity of the proposed algorithm is computed in terms of cost per quantum circuit evaluation and the number of evaluations required until convergence is achieved in classical optimization. The cost of a given circuit is estimated in terms of its depth, which is evaluated by decomposing

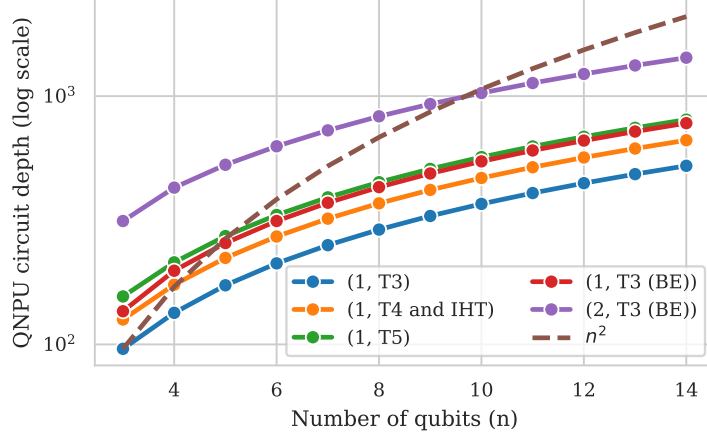


Figure 4: Scaling of QNPU circuit depth (including block-encoding where applicable) with the number of qubits n for different formulations. The depth is shown on a logarithmic scale; the dashed line indicates quadratic scaling $\mathcal{O}(n^2)$. Legend entries denote (shape function order, expansion method).

the circuit into a basis gate set that consists of one- and two-qubit operations (i.e., Hadamard, Pauli, phase, rotation and controlled rotation gates). We utilize *Qiskit Optimization 3* to perform the circuit decompositions.

As per the QNPU framework (see Fig. 1), the total depth (excluding the Hadamard test for simplicity) of a circuit is given by

$$D_c = D_{\text{input}} + D_{\text{QNPU}}, \quad (97)$$

where D_{input} is the depth required by the preparation step (shown as green in Fig. 1) and D_{QNPU} is the depth of the QNPU. If block encoding is used, an additional term D_{BE} is also included (see Fig. 3d). The depth required by the preparation step is given by:

$$D_{\text{input}} = \mathcal{O}(D_{\text{ansatz}}), \quad (98)$$

where D_{ansatz} indicates the depth required to produce one of the controlled input ports and the D_{input} is a small multiple of D_{ansatz} depending on the number of input ports in the circuit. D_{ansatz} itself is dependent on the entanglement structure of the ansatz, the number of repeating layers d and the overhead to implement the ansatz in a controlled way. The scaling of D_{ansatz} is $D_{\text{ansatz}} = \mathcal{O}(nd)$. The contributions from D_{QNPU} (and D_{BE}) are independent of the ansatz structure and their scaling in n is in Fig. 4. The figures indicate $\mathcal{O}(n)$ scaling. Thus we obtain

$$D_c = \mathcal{O}(nd). \quad (99)$$

The total complexity of the algorithm is then expressed as

$$\mathcal{C}_{\text{tot}} = T_{\text{it}} N_{\text{eval/it}} N_{\text{circ/eval}} s D_c, \quad (100)$$

where T_{it} denotes the number of classical optimizer iterations, $N_{\text{eval/it}}$ the number of cost-function evaluations per iteration, $N_{\text{circ/eval}}$ the number of circuits evaluated per cost-function call, and s the number of measurement shots per circuit.

For gradient-based methods, $N_{\text{eval/it}}$ typically scales with the number of variational parameters [39], i.e., $\mathcal{O}(p)$ (or equivalently $\mathcal{O}(nd)$). The number of circuits per evaluation, $N_{\text{circ/eval}}$, depends on the specific formulation but is independent of the problem size. Thus,

$$N_{\text{circ/eval}} = \mathcal{O}(1). \quad (101)$$

In the direct-expansion-based method, $N_{\text{circ/eval}}$ depends on the chosen expansion technique, the approximation order, and the order of the shape functions used in the discretization. In contrast, block-encoding-based approaches can significantly reduce this number, as element-wise arithmetic operations are effectively handled within the block-encoding framework.

The number of measurement shots per circuit, s , depends on the desired accuracy ϵ of the estimated expectation values. In the direct-expansion scheme, the increasing number of circuits may require higher precision per circuit, thereby increasing the shot count. In the block-encoding approach, the number of circuit may be small, however, additional challenges may arise from the post-processing of ancilla measurements. In this work, we adopt a statevector-based simulation approach and therefore do not include shot-noise analysis.

In addition to the contributions mentioned above, the algorithm requires fixed control parameters to prepare several auxiliary states. The number of such states scales as $\mathcal{O}(1)$. For simplicity, we assume that the corresponding control parameters are already known (e.g., from the state-preparation procedure described in Section 4.2), and therefore we do not include their preparation cost in the overall complexity estimate. When combined, the total complexity yields

$$\mathcal{C}_{\text{tot}} = \mathcal{O}\left(T_{\text{it}} \cdot (nd) \cdot N_{\text{circ/eval}} \cdot s \cdot (nd)\right) = \mathcal{O}\left(T_{\text{it}} n^2 d^2 s\right). \quad (102)$$

Comparing against a classical approach where the nonlinear problem is solved using an iterative approach applied on solving a system of equations at each step: the classical cost can be approximated as

$$\mathcal{C}_{\text{cl}} = \mathcal{O}(T_{\text{cl}} \cdot N_q); \quad N_q \sim 2^n, \quad (103)$$

where the Thomas algorithm for tridiagonal systems has a cost of $\mathcal{O}(N_q)$ at each iteration and T_{cl} represents the number of classical iterations. Assuming that d , s and T_{cl} , remain polynomial in n , the proposed quantum framework may exhibit polylogarithmic scaling in the number of classical degrees of freedom N_q , potentially leading to an exponential asymptotic improvement over classical iterative solvers.

6 Numerical Verification

The proposed approach has been implemented in Python. The cost function and Jacobian computations were performed via the quantum algorithm by employing Qiskit 2.2.3. State Vector Simulator method provided by Backend AER without noise was used. The performance and capabilities of the proposed approach have been assessed using a series of numerical experiments discussed below.

BFGS (Broyden–Fletcher–Goldfarb–Shanno) optimization method available within the SciPy Optimization toolkit was used. The cost function gradients were evaluated using finite differences set at default values of $\sqrt{\epsilon_{\text{machine}}}$ [40, 41]. The optimization is terminated when either of the following criteria is satisfied:

$$\left| \mathcal{C}^{(k)} - \mathcal{C}^{(k-1)} \right| < \begin{cases} 10^{-7}, & \text{for three consecutive iterations,} \\ 10^{-8}, & \text{for a single iteration,} \end{cases} \quad (104)$$

where $\mathcal{C}^{(k)}$ denotes the value of the cost function (17) at iteration k . The effect of stopping criteria is demonstrated using an example in Section 6.2.

The initial guess for the control parameters used in the cost-function optimization are selected such that the resulting displacement profile satisfies the constraint (26b). Accordingly, random displacement profiles are generated such that $-\alpha < u' < \alpha$, $\alpha = 0.5$. Control parameters for a profile that satisfies this constraint are created using the state-preparation procedure described in Section 4.2. For the IHT-based formulation, the initial guess for the u profile (and the associated control parameters) was generated using the same procedure, while the y profile (and its corresponding control parameters) was obtained using (31).

The errors in the approximated solutions stem from two sources. The first is the polynomial approximation of the nonlinear logarithmic term in (21), which introduces a theoretical modeling error. Consequently, the algorithm computes the solution corresponding to the approximated strain energy density function instead of the original hyperelastic model. Accordingly, we report the maximum deviation in displacement gradient and the L_2 displacement error (relative to the analytical solution of (21) u^{NLS} – percentage measure):

$$E_{|u'|}^{\text{NLS}} = \max_{X \in \Omega_0} |u^{\text{VQ}'}(X) - u^{\text{NLS}'}(X)|, \quad E_{L_2}^{\text{NLS}} = \frac{\left(\int_{\Omega_0} |u^{\text{VQ}}(X) - u^{\text{NLS}}(X)|^2 dX\right)^{1/2}}{\left(\int_{\Omega_0} |u^{\text{NLS}}(X)|^2 dX\right)^{1/2}} \times 100, \quad (105)$$

where u^{VQ} represents the FE field for displacement obtained using the VQA approach. The second source of error arises from the introduction of VQA itself. To isolate this error, we measure the fidelity of the quantum state obtained from the VQA relative to a reference state, generated by minimizing the same energy functional classically, directly for the displacement field. We refer to the quantum state of the classically obtained reference profile as $|\hat{u}^{\text{Cl}}\rangle$ and compute the fidelity as:

$$E_{\text{tr}}^{\text{Cl}} = \sqrt{1 - |\langle \hat{u}^{\text{VQ}} | \hat{u}^{\text{Cl}} \rangle|^2}, \quad (106)$$

where $|\hat{u}^{\text{VQ}}\rangle$ represents the quantum state obtained using the optimal quantum parameters based on the chosen ansatz.

All errors are evaluated over a sample of 20 successful independent runs per example. In each run, both the classical optimization and the VQA-based optimization are initialized using the same initial guess for the classical DoFs \mathbf{u} (and auxiliary variables \mathbf{y} , where applicable), chosen within the admissible bounds. The reported values correspond to averages over these runs.

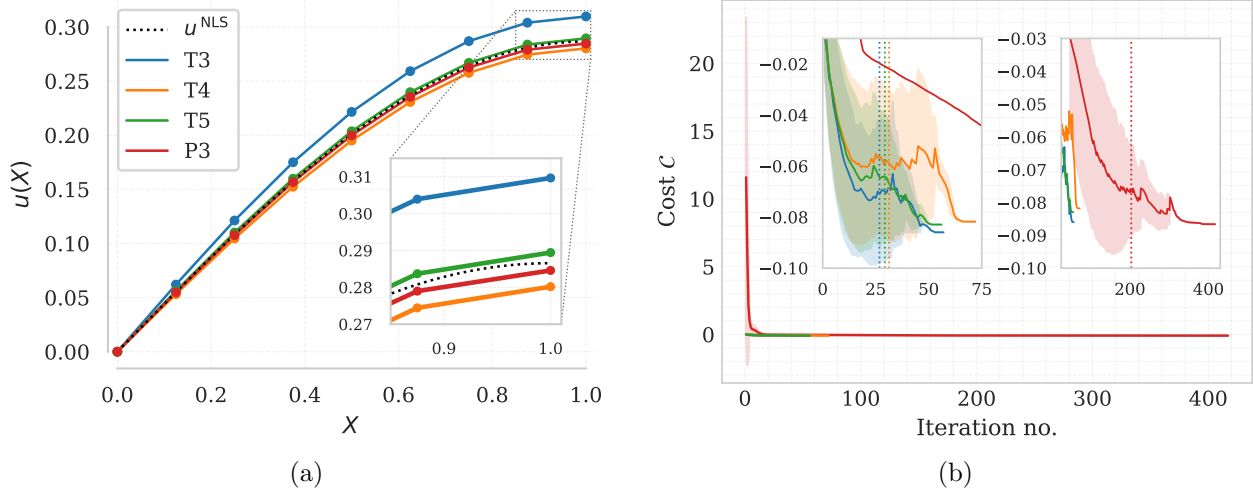
6.1 Effect of nonlinearity approximation

In this section, the accuracy and computational costs of the proposed method are investigated relative to the polynomial approximation of the logarithmic term in the Neo-Hookean strain energy density function. Consider a domain of unit length ($L = 1$ mm) discretized into 8 first-order (i.e., linear) elements (with 8 DoFs excluding the Dirichlet boundary node) using a uniform finite element grid. The domain is subjected to a linear body force

$$B(X) = \kappa X, \quad (107)$$

and traction free boundary at $X = L$ (i.e., $\bar{P} = 0$ N/mm²). The modulus and the body force constants are set to $\mu = 1$ MPa and $\kappa = 1.5$ N/mm⁴.

Figure 5 shows the predicted displacement profiles and the evolution of the cost function as a function of optimization iterations for Taylor series and IHT approximations. The internal DoFs are



	Evaluations	$E_{L_2}^{\text{NLS}}(\%)$	$E_{ u' }^{\text{NLS}}$	$E_{\text{tr}}^{\text{Cl}}$
T3	403 ± 161	$8.92 \pm 2.41 \times 10^{-3}$	$6.09 \times 10^{-2} \pm 2.89 \times 10^{-5}$	$1.89 \times 10^{-5} \pm 1.36 \times 10^{-5}$
T4	444 ± 208	$2.86 \pm 9.75 \times 10^{-3}$	$4.59 \times 10^{-2} \pm 1.42 \times 10^{-5}$	$2.07 \times 10^{-5} \pm 1.79 \times 10^{-5}$
T5	432 ± 159	$0.92 \pm 7.90 \times 10^{-3}$	$4.59 \times 10^{-2} \pm 5.91 \times 10^{-5}$	$4.11 \times 10^{-5} \pm 1.57 \times 10^{-5}$
P3	4699 ± 1635	$0.9 \pm 3.19 \times 10^{-2}$	$4.62 \times 10^{-2} \pm 4.40 \times 10^{-3}$	$6.13 \times 10^{-4} \pm 1.56 \times 10^{-3}$

(c)

Figure 5: VQA performance (20-run average) for Taylor orders 3–5 (T3–T5) and IHT (P3). The profiles of u^{VQ} (in mm) and the iteration cost histories are shown in (a) and (b), respectively. Performance metrics for the different models are summarized in Table (c), where “Evaluations” denotes the average number of function calls over the entire optimization process.

represented using a 3-qubit main register ($n = 3$). The ansatz layer depth is set to $d = 2$ resulting in 10 control parameters for the models that use Taylor approximations, and 20 (10 for displacement and 10 for auxiliary field) for the model that uses IHT approximation. Three models use Taylor series approximations (T3, T4, T5 with three, four and five term expansions, respectively), whereas the model with IHT approximation (P3) employs expansion up to and including the cubic term. The total number of distinct circuits required for T3, T4, T5, and P3 are 7, 11, 16, and 21, respectively. The most expensive circuits for these cases require 11, 14, 17, and 14 qubits, respectively. The P3 model uses a penalty parameter of $\mathcal{P} = 10^2$.

The displacement profiles in Fig. 5a, together with the L_2 errors listed in Table 5c, show that the numerical solution approaches the non-linear analytical solution as the order of the polynomial approximation increases. The analytical solution to the problem is derived in Appendix A.2. The small trace errors indicate that the computed profiles u^{VQ} closely match the expected profiles that would be obtained using a classical minimizer applied to the approximated energy functional. Among the considered methods, the IHT-based method yields the most accurate results. However, the IHT-based method exhibits convergence difficulties, reflected in larger standard deviations of the error metrics and slower convergence in Fig. 5b, especially near the minimizer. These convergence difficulties are attributed to the penalty formulation, specifically the ill conditioning introduced by the penalty parameter, \mathcal{P} . Setting small values to \mathcal{P} lead to ineffective enforcement of constraint, whereas large values can cause ill-conditioning as is well known in optimization literature [41].

Figure 6 demonstrates that polynomial approximations can degrade the convexity of the potential energy functional, leading to divergence, convergence to nonphysical solutions, or optimization trajectories entering regions where $u' < -1$. To quantify this behavior, κ in (107) is varied and the corresponding success ratio (fraction of initial guesses that converge under the prescribed optimization criteria) and $E_{L_2}^{\text{NLS}}$ are evaluated. The resulting success rates (computed over 100 runs) and errors (computed over 20 successful runs) are reported in Fig. 6a and Fig. 6b, respectively. Among the Taylor expansions, the fourth-order approximation preserves convexity more effectively than the third- and fifth-order approximations, yielding consistently higher success rates. However, its accuracy deteriorates for larger α , with $E_{L_2}^{\text{NLS}}$ reaching approximately 15% at $\kappa = 3$. Beyond $\kappa \geq 3$, analytical solution demands $u' > 1$, invalidating the Taylor expansion based models. In contrast, the third-order IHT expansion performs well away from $\alpha \approx 0$ but exhibits lower success rates and larger errors near this regime. Overall, Taylor expansions are better suited for small deformations, whereas the IHT-based expansion performs more reliably for larger deformations.

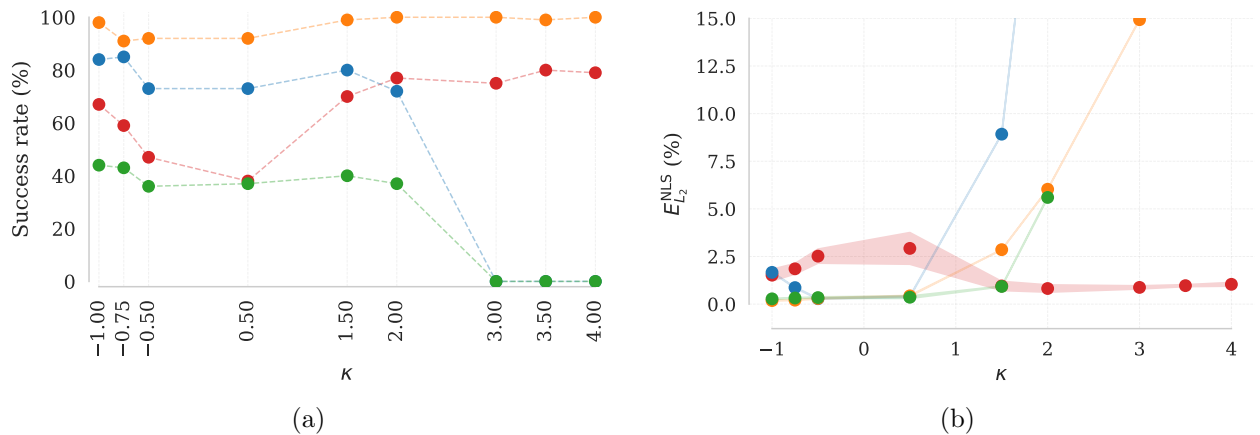
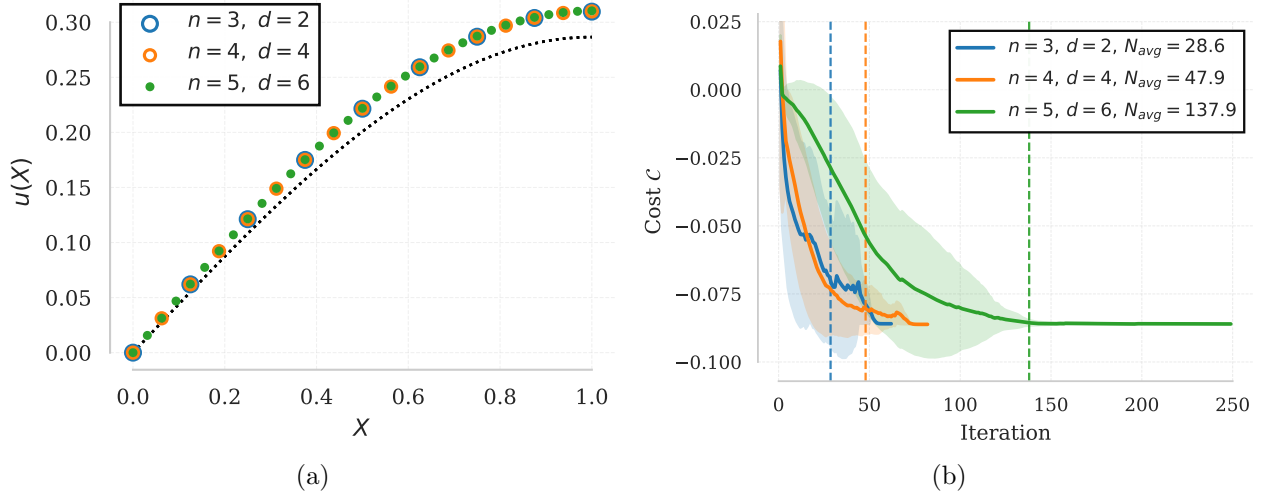


Figure 6: Performance of different models as a function of κ (N/mm⁴)(see (107)), averaged over 100 runs: (a) success rate and (b) L_2 error relative to the analytical solution.

6.2 Effect of problem size

In this section, the characteristics of the solution process as a function of the problem size are investigated. We report scaling results only for the Taylor expansion method up to the third order. Higher-order expansions require additional ancilla qubits that significantly increase the size of the state vector and the associated memory cost. This makes large problems difficult to implement on classical simulators. Although approaches have been recently proposed to alleviate these limitations to some extent [1], they are not considered in the present work.

Figure 7 shows the results obtained for the problem setting discussed in the previous section, but with three increasingly refined meshes. Internal DoF encoded in the main qubit register are $n = 3, 4, 5$ with variational ansatz layer depths set to $d = 2, 4$, and 6, respectively. The number of distinct circuits is independent of the number of qubits, whereas the size of the most expensive circuit scales as $4n - 1$. As mesh refinement increases the problem size and enlarges the displacement vector, a richer ansatz is required to adequately parameterize the solution space and to retain expressivity. The minimum depths selected for each value of n are those required to achieve trace errors below 10^{-3} . Increasing the circuit depth (and thus the number of parameters) does not significantly affect the metrics for $n = 3$ and $n = 4$. However, for $n = 5$, improvements across all



n	d	p	Avg. Func. Calls	$E_{L_2}^{\text{NLS}}$	$E_{ u' }^{\text{NLS}}$	$E_{\text{tr}}^{\text{Cl}}$
3	2	9	399 ± 180	$8.9 \pm 1.9 \times 10^{-3}$	$6.1 \times 10^{-2} \pm 6.2 \times 10^{-5}$	$1.3 \times 10^{-5} \pm 7.7 \times 10^{-6}$
3	4	15	601 ± 224	$8.9 \pm 2.3 \times 10^{-3}$	$6.1 \times 10^{-2} \pm 4.8 \times 10^{-5}$	$1.4 \times 10^{-5} \pm 1.5 \times 10^{-5}$
4	4	20	1277 ± 373	$9.2 \pm 2.4 \times 10^{-2}$	$5.8 \times 10^{-2} \pm 1.8 \times 10^{-4}$	$3.5 \times 10^{-5} \pm 2.3 \times 10^{-5}$
4	6	28	1828 ± 482	$9.2 \pm 1.5 \times 10^{-2}$	$5.8 \times 10^{-2} \pm 1.1 \times 10^{-4}$	$3.1 \times 10^{-5} \pm 2 \times 10^{-5}$
5	6	35	5731 ± 1722	$9.4 \pm 8.3 \times 10^{-1}$	$6.4 \times 10^{-2} \pm 1.1 \times 10^{-2}$	$9.9 \times 10^{-4} \pm 9.7 \times 10^{-4}$
5	8	45	4761 ± 1113	$9.3 \pm 10 \times 10^{-2}$	$5.8 \times 10^{-2} \pm 6.6 \times 10^{-4}$	$1.4 \times 10^{-4} \pm 5.6 \times 10^{-5}$

(c)

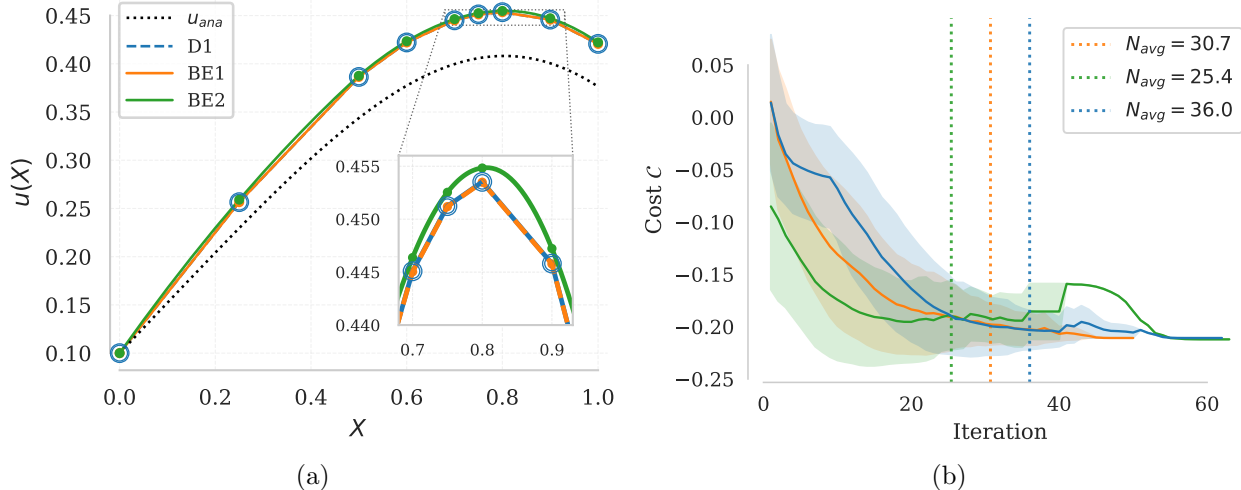
Figure 7: VQA scaling for $n = 3, 4$, and 5 qubits using a third-order Taylor expansion (20-run average). The profiles of u^{VQ} (in mm) and the iteration-cost histories are shown in (a) and (b), respectively. Performance metrics are summarized in Table (c). Vertical dotted lines in (b) indicate the average convergence iterations N_{avg} for the minimum ansatz layer depth required by each value of n .

reported metrics (see Table 7c) indicate that systems with a larger number of qubits may require additional parameters to achieve better performance.

Figure 7a shows that the displacement profiles obtained using the VQA approach converge to the same global solution upon refinement, while Fig. 7b presents the corresponding optimization histories. No barren plateau behavior has been observed within the current setup. However, refinement introduces convergence difficulties near the minimizer. When the stopping criterion (104) is relaxed, larger systems require extremely small cost variations over many iterations before gradients vanish, often exceeding machine precision limits and preventing further optimization. This is also evident from the long tail that is noticeable in the optimization history for $n = 5$. In contrast, smaller systems converge within a reasonable precision tolerance.

6.3 Assessment of robustness

In this section, several additional aspects of the model implementation are evaluated. We consider the following setup: The problem domain is discretized using two non-uniform meshes. The first mesh consists of eight linear finite elements with element lengths (in mm) of $[0.25, 0.25, 0.1, 0.1, 0.05, 0.05, 0.1, 0.1]$. The second mesh consists of four quadratic finite elements with element lengths



Formulation	Evaluations	$E_{L_2}^{\text{NLS}}$ (%)	$E_{ u' }^{\text{NLS}}$	$E_{\text{tr}}^{\text{Cl}}$
BE1	454 ± 115	$11 \pm 9.8 \times 10^{-3}$	$0.14 \pm 1.1 \times 10^{-4}$	$2.4 \times 10^{-5} \pm 1.3 \times 10^{-5}$
BE2	402 ± 149	$12 \pm 2 \times 10^{-2}$	$0.13 \pm 2.2 \times 10^{-4}$	$9.6 \times 10^{-5} \pm 4.4 \times 10^{-5}$
D1	652 ± 148	$11 \pm 1.6 \times 10^{-2}$	$0.14 \pm 1.2 \times 10^{-4}$	$3.6 \times 10^{-5} \pm 2.8 \times 10^{-5}$

(c)

Figure 8: VQA performance comparison for different formulations (20-run average). The formulation notation denotes BE1 and BE2 as the block-encoding-based approaches employing first- and second-order shape functions, respectively, while D1 denotes the direct-expansion-based approach employing first-order shape functions. The profiles of u^{VQ} (in mm) and the iteration-cost histories are shown in (a) and (b), respectively. Vertical dotted lines in (b) indicate the average convergence iterations N_{avg} . Performance metrics are summarized in Table (c).

of $[0.5, 0.2, 0.1, 0.2]$. The internal DoFs for both meshes are encoded in a 3-qubit main register ($n = 3$). The domain is subjected to a quadratic body force (i.e., $B(X) = 5X^2$ N/mm³, X in mm) with a prescribed traction at $X = L$ ($\bar{P} = -0.8$ N/mm²) and a non-homogeneous Dirichlet condition at $X = 0$ ($\bar{u} = 0.1$ mm). The modulus of the domain is set to $\mu = 1$ MPa. The logarithmic nonlinearity in the strain energy density is approximated using a three-term Taylor series approximation. In case of the mesh with linear elements, both direct expansion (D1) and Block encoding-based (BE1) approaches were used to establish the circuits associated with the resulting cost function. In case of the mesh with quadratic elements, the Block encoding (BE2) scheme was used.

Figure 8 presents the displacement fields and optimization histories obtained using the proposed approach. The two linear discretization models exhibit comparable convergence behavior and error characteristics, as summarized in Table 8c. In contrast, the second-order shape function model yields larger errors, which may be attributed to the use of only two Gauss integration points. Compared to the analytical solution, the errors observed in this example are higher than those reported in the preceding cases, as the present problem was intentionally selected to assess the limitations of the proposed scheme. Nevertheless, the low trace errors across all formulations indicate accurate solution recovery by the VQA approach.

From a structural perspective, the block-encoding approaches (BE1 and BE2) require only 3 cir-

circuits compared to 11 for the direct approach, albeit with additional ancilla and post-measurement overheads. The largest BE1 and BE2 circuits require 15 and 17 qubits, with 6 and 4 post-measurements, respectively (Section 4.1.4), posing a challenge towards their implementation. Similar to the example in Section 6.2, upon relaxing the optimization criterion in Eq. (104), it was observed that the non-uniform mesh configuration requires substantially higher cost-function precision before the gradient norm falls below the prescribed tolerance.

7 Conclusion

This manuscript presented a variational quantum algorithm (VQA)–based framework for solving nonlinear elasticity problems arising from hyperelastic material models. The proposed approach approximates nonlinearities in the strain energy density using polynomial expansions, enabling their implementation on quantum hardware via Quantum Nonlinear Processing Units (QNPU). The methodology was demonstrated on a one-dimensional Neo-Hookean problem, where the potential energy functional is used as the VQA cost function. Two types of polynomial approximations were investigated, and the VQA was shown to capture the expected behavior using both first- and second-order finite element discretizations on non-uniform meshes with non-homogeneous boundary conditions.

The study highlights several practical challenges, including the influence of polynomial approximations on accuracy, convergence difficulties in more complex formulations, and increased computational cost associated with higher-order expansions and auxiliary variables. In addition, current implementations are limited by the cost of statevector simulations, particularly for larger problem sizes, restricting the analysis of scaling behavior. Future work will focus on addressing these limitations. In particular, developing more efficient approximation strategies that balance accuracy with quantum resource requirements (such as circuit depth and ancilla usage) is of primary interest. Extending the framework to a broader class of nonlinearities while maintaining quantum compatibility and implementing the proposed approach on current and near-term quantum hardware will be explored, requiring modifications to the algorithmic structure.

CRedit authorship contribution statement

Uditnarayan Kouskiya: Conceptualization, Methodology, Software, Formal analysis, Investigation, Data curation, Visualization, Writing – original draft, Writing – review & editing. Caglar Oskay: Conceptualization, Supervision, Methodology, Formal analysis, Writing – review & editing, Project administration, Funding acquisition.

Data availability

Data supporting the findings of this study are available from the corresponding author upon reasonable request.

Declaration of competing interest

The authors declare that they have no known competing financial interests or personal relationships that could have appeared to influence the work reported in this manuscript.

Acknowledgments

The authors gratefully acknowledge the funding support from the National Science Foundation, CMMI Division, Mechanics of Materials and Structures Program, United States of America (Award No: 2222404 and No: 2527249).

A Solution to the simplified Neo-hookean model

A.1 Existence and Uniqueness of the Minimizer

Consider the energy functional introduced in Section 3:

$$\mathcal{E}[u] = \int_{\Omega_0} \left[\mu \left(u' + \frac{1}{2}(u')^2 - \ln(1 + u') \right) - B u \right] dX - \sum_{X \in \Gamma_N} \bar{P} u(X). \quad (108)$$

with $u(X) = \bar{u}$ for $X \in \Gamma_D$. For

$$\mathcal{V}_0 := \{v \in H^1(\Omega_0) : v = 0 \text{ on } \Gamma_D\},$$

the first variation of \mathcal{E} in the direction $v \in \mathcal{V}_0$ is given by

$$\delta\mathcal{E}[u; v] = \lim_{\epsilon \rightarrow 0} \frac{\mathcal{E}[u + \epsilon v] - \mathcal{E}[u]}{\epsilon}. \quad (109)$$

A direct computation yields

$$\delta\mathcal{E}[u; v] = \int_{\Omega_0} P(\lambda) v' dX - \int_{\Omega_0} B(X) v dX - \sum_{X \in \Gamma_N} \bar{P} v(X), \quad (110)$$

where

$$\lambda = 1 + u', \quad P(\lambda) = \mu (\lambda - \lambda^{-1}). \quad (111)$$

Thus, the condition

$$\delta\mathcal{E}[u; v] = 0 \quad \forall v \in \mathcal{V}_0 \quad (112)$$

is equivalent to the weak form of the governing equations presented in Section 2.1. Under sufficient smoothness, the last equation implies that u satisfies the strong form. Consider the second variation of \mathcal{E} , in the direction $w \in \mathcal{V}_0$:

$$\delta^2\mathcal{E}[u; v, w] = \int_{\Omega_0} \mu (1 + (1 + u')^{-2}) v'(X) w'(X) dX. \quad (113)$$

By setting $w = v$, we obtain

$$\delta^2\mathcal{E}[u; v, v] = \int_{\Omega_0} \mu (1 + (1 + u')^{-2}) (v'(X))^2 dX.$$

Since physical admissibility requires $\lambda = 1 + u' > 0$, we obtain

$$1 + (1 + u')^{-2} > 0.$$

Hence, for $\mu > 0$, the integrand in (113) is strictly positive for any $v \neq 0$, which implies

$$\delta^2\mathcal{E}[u; v, v] > 0 \quad \forall v \in \mathcal{V}_0, v \neq 0.$$

Therefore, the second variation defines a positive definite bilinear form on \mathcal{V}_0 , and the energy functional \mathcal{E} is strictly convex over the admissible space. Consequently, the minimizer of \mathcal{E} is unique and also represents the solution of the weak form (112).

A.2 Exact Solution of the Strong Form

Based on the examples considered in this work, we consider a Dirichlet condition at $X = 0$ and a Neumann (traction) condition at $X = L$, i.e.,

$$\Gamma_D = \{0\}, \quad \Gamma_N = \{L\}.$$

The strong form of the governing equation is

$$\frac{d}{dX} P(\lambda(X)) + B(X) = 0, \quad (114)$$

Integrating (114) from X to L , and using the boundary condition $P(\lambda(L)) = \bar{P}$, we obtain

$$P(\lambda(X)) = \int_X^L B(s) ds + \bar{P}. \quad (115)$$

Substituting the constitutive relation from (111) gives

$$\mu \left(\lambda(X) - \frac{1}{\lambda(X)} \right) = \int_X^L B(s) ds + \bar{P}.$$

Define

$$H(X) := \frac{1}{\mu} \int_X^L B(s) ds + \frac{\bar{P}}{\mu}.$$

Then the governing relation becomes

$$\lambda - \frac{1}{\lambda} = H. \quad (116)$$

Solving (116) for λ yields

$$\lambda(X) = \frac{1}{2} \left(H(X) \pm \sqrt{H(X)^2 + 4} \right). \quad (117)$$

The physically admissible solution corresponds to $\lambda > 0$, hence

$$u'(X) = \lambda(X) - 1.$$

Integrating and applying the Dirichlet boundary condition $u(0) = \bar{u}$, we obtain

$$u(X) = \bar{u} + \int_0^X \left[\frac{1}{2} \left(H(s) + \sqrt{H(s)^2 + 4} \right) - 1 \right] ds. \quad (118)$$

B Cost function implementation for IHT expansion

For the functional (30), we employ a first order finite element discretization for u and approximate y using a piecewise constant field over the mesh. Specifically, we write

$$y(x) \approx \tilde{y}(x) = \sum_{e=0}^{N_q-1} y_e \chi_e(x), \quad (119)$$

where χ_e denotes the characteristic function of element Ω_e . With these settings, the approximation of energy (30) based on a two-point Gauss quadrature can be given by:

$$\tilde{\mathcal{E}}(\mathbf{u}, \mathbf{y}) = \sum_{e=0}^{N_q-1} h_e \left[u'_e + \frac{1}{2} (u'_e)^2 - 2 \left(y_e + \frac{1}{3} y_e^3 \right) + \frac{\mathcal{P}}{2} (y_e (u'_e + 2) - u'_e)^2 \right] - \tilde{\mathcal{E}}_B(\mathbf{u}); \quad (120)$$

$$u'_e := \frac{u_{2e} - u_{1e}}{h_e}; \quad \tilde{\mathcal{E}}_B(\mathbf{u}) = \sum_{e=0}^{N_q-1} \sum_{g=0}^1 \frac{h_e}{2} B(X^{(g)}) \tilde{u}(X^{(g)}).$$

The penalty term for any element can be expanded as:

$$\frac{\mathcal{P}}{2} (y_e (u'_e + 2) - u'_e)^2 = \frac{\mathcal{P}}{2} \left(y_e^2 (u'_e)^2 + 4y_e^2 + (u'_e)^2 + 4y_e^2 u'_e - 2y_e (u'_e)^2 - 4y_e u'_e \right).$$

Let $\mathbf{u} = (\bar{u}, \mathbf{v})$ be represented using control parameters as defined in (68). Similarly let $\mathbf{y} \in \mathbb{R}^{N_q}$ be represented using:

$$\mathbf{y} = \theta_0 \widehat{V}(\boldsymbol{\theta}).$$

A few terms in (120) are treated in the main text in Section 4.3. The remaining terms up to scaling factors, in the quantum-computing-implementable form are written below:

$$\begin{aligned} \sum_{e=0}^{N_q-1} h_e u'_e &= u_{N_q} - u_0 = \lambda_0 \langle \hat{v} | \hat{m}^{(-1)} \rangle - \bar{u}; \quad -2 \sum_{e=0}^{N_q-1} h_e y_e = -2 \mathbf{h}^\top \mathbf{y} = -2 \theta_0 \|\mathbf{h}\| \langle \hat{h} | \hat{v} \rangle; \\ -\frac{2}{3} \sum_{e=0}^{N_q-1} h_e y_e^3 &= -\frac{2}{3} \mathbf{y}^\top (\mathbf{h} \odot \mathbf{y} \odot \mathbf{y}) = -\frac{2}{3} \theta_0^3 \|\mathbf{h}\| \langle \hat{v} | D_{\hat{h}} D_{\hat{v}} | \hat{v} \rangle; \\ 2\mathcal{P} \sum_{e=0}^{N_q-1} h_e y_e^2 &= 2\mathcal{P} \mathbf{y}^\top (\mathbf{h} \odot \mathbf{y}) = 2\mathcal{P} \theta_0^2 \|\mathbf{h}\| \langle \hat{v} | D_{\hat{h}} | \hat{v} \rangle. \end{aligned}$$

The term

$$\frac{\mathcal{P}}{2} \sum_{e=0}^{N_q-1} h_e (u'_e)^2 y_e^2 = \frac{\mathcal{P}}{2} \underbrace{\left(\frac{\bar{u}^2 - 2\bar{u} u_1 + u_1^2}{h_0} y_0^2 \right)}_{\text{element 1 contribution}} + T_{\text{bulk}},$$

where

$$\begin{aligned} u_1 = v_0 &= \langle \hat{v} | \hat{m}^{(1)} \rangle; \quad y_0 = \langle \hat{y} | \hat{m}^{(1)} \rangle; \\ T_{\text{bulk}} &= \lambda_0^2 \theta_0^2 \|\mathbf{m}^{(9)}\| \left(\langle \hat{v} | D_{\hat{y}}^2 D_{\hat{m}^{(9)}} | \hat{v} \rangle + \langle \hat{A} \hat{v} | D_{\hat{y}}^2 D_{\hat{m}^{(9)}} | \hat{A} \hat{v} \rangle + \langle \hat{v} | D_{\hat{y}}^2 D_{\hat{m}^{(9)}} \hat{A} | \hat{v} \rangle \right) \end{aligned}$$

and

$$m_i^{(9)} = \begin{cases} 0, & i = 0, \\ \frac{1}{h_i}, & i = 1, \dots, N_q - 1. \end{cases}$$

Similarly,

$$\begin{aligned}
-\mathcal{P} \sum_{e=0}^{N_q-1} h_e (u'_e)^2 y_e &= -\mathcal{P} \left(\frac{\bar{u}^2 - 2\bar{u} u_1 + u_1^2}{h_0} y_0 \right) \\
&\quad + \lambda_0^2 \theta_0 \|\mathbf{m}^{(9)}\| \left(\langle \hat{v} | D_{\hat{y}} D_{\hat{m}^{(9)}} | \hat{v} \rangle + \langle \hat{A} \hat{v} | D_{\hat{y}} D_{\hat{m}^{(9)}} | \hat{A} \hat{v} \rangle + \langle \hat{v} | D_{\hat{y}} D_{\hat{m}^{(9)}} \hat{A} | \hat{v} \rangle \right). \quad (121)
\end{aligned}$$

We also have

$$\begin{aligned}
2\mathcal{P} \sum_{e=0}^{N_q-1} h_e y_e^2 u'_e &= -2\mathcal{P} \left(\bar{u} y_0^2 - \lambda_0 \theta_0^2 \langle \hat{y} | D_{\hat{v}} | \hat{y} \rangle + \|\mathbf{m}^{(10)}\| \langle \hat{y} | D_{\hat{v}} D_{\hat{m}^{(10)}} \hat{A} | \hat{y} \rangle \right) \text{ and} \\
-2\mathcal{P} \sum_{e=0}^{N_q-1} h_e y_e u'_e &= 2\mathcal{P} \left(\bar{u} y_0 - \lambda_0 \theta_0 \langle \hat{y} | \hat{v} \rangle + \|\mathbf{m}^{(10)}\| \langle 0 | \hat{V}^\dagger(\boldsymbol{\lambda}) D_{\hat{m}^{(10)}} \hat{A} \hat{V}(\boldsymbol{\theta}) | 0 \rangle \right),
\end{aligned}$$

where $\mathbf{m}^{(10)} = [0, 1, 1 \cdots 1]$.

References

- [1] Kaijie Wei et al. “A data compressor for FPGA-based state vector quantum simulators”. In: *Proceedings of the 14th International Symposium on Highly Efficient Accelerators and Reconfigurable Technologies*. HEART '24. Porto, Portugal: Association for Computing Machinery, 2024, pp. 63–70. ISBN: 9798400717277. DOI: 10.1145/3665283.3665293. URL: <https://doi.org/10.1145/3665283.3665293>.
- [2] Zebo Yang, Maede Zolanvari, and Raj Jain. “A Survey of Important Issues in Quantum Computing and Communications”. In: *IEEE Communications Surveys & Tutorials* 25.2 (2023). A broad survey of architectures, algorithms, and challenges in quantum computing and communication., pp. 1059–1100. DOI: 10.1109/COMST.2023.3241234.
- [3] Andrew M. Childs, Jin-Peng Liu, and Aaron Ostrander. “Improved Quantum Algorithms for Linear and Nonlinear Differential Equations”. In: *Quantum* 7 (2023). High-level development of quantum algorithms for both linear and nonlinear differential equations., p. 913. DOI: 10.22331/q-2023-02-02-913.
- [4] Giorgio Tosti Balducci et al. “Review and perspectives in quantum computing for partial differential equations in structural mechanics”. In: *Frontiers in Mechanical Engineering* Volume 8 - 2022 (2022). ISSN: 2297-3079. DOI: 10.3389/fmech.2022.914241. URL: <https://www.frontiersin.org/journals/mechanical-engineering/articles/10.3389/fmech.2022.914241>.
- [5] Dominic W. Berry. *Quantum algorithm for linear differential equations*. arXiv:1701.03684. 2017.
- [6] Jin-Peng Liu. “Quantum Algorithms for Linear and Nonlinear Differential Equations”. PhD thesis. University of Maryland, 2022.
- [7] Aram W. Harrow, Avinatan Hassidim, and Seth Lloyd. “Quantum Algorithm for Linear Systems of Equations”. In: *Physical Review Letters* 103.15 (2009), p. 150502. DOI: 10.1103/PhysRevLett.103.150502.
- [8] Seth Lloyd. “Universal Quantum Simulators”. In: *Science* 273.5278 (1996), pp. 1073–1078. DOI: 10.1126/science.273.5278.1073.
- [9] Dominic W. Berry and Andrew M. Childs. “Hamiltonian simulation using linear combinations of unitary operations”. In: *Quantum Information and Computation* 12 (2012), pp. 29–62.
- [10] John M. Martyn et al. “A Grand Unification of Quantum Algorithms”. In: *PRX Quantum* 2 (2021), p. 040203. DOI: 10.1103/PRXQuantum.2.040203.
- [11] Yigit Subaşı, Rolando D. Somma, and Davide Orsucci. “Quantum Algorithms for Systems of Linear Equations Inspired by Adiabatic Quantum Computing”. In: *Physical Review Letters* 122.6 (2019), p. 060504. DOI: 10.1103/PhysRevLett.122.060504.
- [12] Yudong Cao et al. “Quantum algorithm and circuit design solving the Poisson equation”. In: *New Journal of Physics* 15.1 (2013), p. 013021. DOI: 10.1088/1367-2630/15/1/013021.
- [13] Ashley Montanaro and Sam Pallister. “Quantum algorithms and the finite element method”. In: *Physical Review A* 93.3 (2016), p. 032324. DOI: 10.1103/PhysRevA.93.032324.
- [14] John Preskill. “Quantum Computing in the NISQ era and beyond”. In: *Quantum* 2 (2018), p. 79. DOI: 10.22331/q-2018-08-06-79.

- [15] Kishor Bharti et al. “Noisy intermediate-scale quantum algorithms”. In: *Rev. Mod. Phys.* 94 (1 Feb. 2022), p. 015004. DOI: 10.1103/RevModPhys.94.015004. URL: <https://link.aps.org/doi/10.1103/RevModPhys.94.015004>.
- [16] Alberto Peruzzo et al. “A variational eigenvalue solver on a photonic quantum processor”. In: *Nature Communications* 5.1 (2014), p. 4213. DOI: 10.1038/ncomms5213. URL: <https://doi.org/10.1038/ncomms5213>.
- [17] Carlos Bravo-Prieto et al. “Variational Quantum Linear Solver”. In: *Quantum* 7 (Nov. 2023), p. 1188. DOI: 10.22331/q-2023-11-22-1188. URL: <https://doi.org/10.22331/q-2023-11-22-1188>.
- [18] A. Arora, B. M. Ward, and C. Oskay. “An implementation of the finite element method in hybrid classical/quantum computers”. In: *Finite Elements in Analysis and Design* 248 (2025), p. 104354.
- [19] Xiang Rao and Kou Du. “Performance Study of Variational Quantum Linear Solver for Linear Elastic Problems”. In: *Computational and Experimental Simulations in Engineering*. Ed. by Kun Zhou. Vol. 168. Mechanisms and Machine Science. Cham: Springer, 2024, pp. 80–94. ISBN: 978-3-031-68775-4. DOI: 10.1007/978-3-031-68775-4_6.
- [20] Katsuhiko Endo and Kazuaki Z. Takahashi. “Divergence-free algorithms for solving nonlinear differential equations on quantum computers”. In: *Phys. Rev. Res.* 8 (1 Jan. 2026), p. 013057. DOI: 10.1103/2hfp-qyz1. URL: <https://link.aps.org/doi/10.1103/2hfp-qyz1>.
- [21] Yongchun Xu et al. “A robust quantum nonlinear solver based on the asymptotic numerical method”. In: *arXiv preprint arXiv:2412.03939* (2024). DOI: 10.48550/arXiv.2412.03939. URL: <https://arxiv.org/abs/2412.03939>.
- [22] Michael Lubasch et al. “Variational quantum algorithms for nonlinear problems”. In: *Phys. Rev. A* 101 (1 Jan. 2020), p. 010301. DOI: 10.1103/PhysRevA.101.010301. URL: <https://link.aps.org/doi/10.1103/PhysRevA.101.010301>.
- [23] Abhijat Sarma et al. “Quantum variational solving of nonlinear and multidimensional partial differential equations”. In: *Phys. Rev. A* 109 (6 June 2024), p. 062616. DOI: 10.1103/PhysRevA.109.062616. URL: <https://link.aps.org/doi/10.1103/PhysRevA.109.062616>.
- [24] Yuki Sato et al. “Variational quantum algorithm based on the minimum potential energy for solving the Poisson equation”. In: *Phys. Rev. A* 104 (5 Nov. 2021), p. 052409. DOI: 10.1103/PhysRevA.104.052409. URL: <https://link.aps.org/doi/10.1103/PhysRevA.104.052409>.
- [25] Paul Over et al. “Boundary treatment for variational quantum simulations of partial differential equations on quantum computers”. In: *Computers and Fluids* 288 (2025), p. 106508. ISSN: 0045-7930. DOI: <https://doi.org/10.1016/j.compfluid.2024.106508>. URL: <https://www.sciencedirect.com/science/article/pii/S0045793024003396>.
- [26] Sergio Bengoechea, Paul Over, and Thomas Rung. “Quantum time-marching algorithms for solving linear transport problems including boundary conditions”. In: *arXiv preprint arXiv:2511.04271* (2025). DOI: 10.48550/arXiv.2511.04271. arXiv: 2511.04271 [quant-ph]. URL: <https://arxiv.org/abs/2511.04271>.
- [27] Jerrold E Marsden and Thomas JR Hughes. *Mathematical Foundations of Elasticity*. Dover Publications, 1994.

- [28] Sukin Sim, Peter D. Johnson, and Alán Aspuru-Guzik. “Expressibility and Entangling Capability of Parameterized Quantum Circuits for Hybrid Quantum-Classical Algorithms”. In: *Advanced Quantum Technologies* 2.12 (2019), p. 1900070. DOI: <https://doi.org/10.1002/qute.201900070>. eprint: <https://advanced.onlinelibrary.wiley.com/doi/pdf/10.1002/qute.201900070>. URL: <https://advanced.onlinelibrary.wiley.com/doi/abs/10.1002/qute.201900070>.
- [29] Arthur G. Rattew and Patrick Reberstrost. *Non-Linear Transformations of Quantum Amplitudes: Exponential Improvement, Generalization, and Applications*. 2023. arXiv: 2309.09839 [quant-ph]. URL: <https://arxiv.org/abs/2309.09839>.
- [30] Milton Abramowitz and Irene A. Stegun. *Handbook of Mathematical Functions with Formulas, Graphs, and Mathematical Tables*. Vol. 55. Applied Mathematics Series. Washington, D.C.: National Bureau of Standards, 1964.
- [31] Karel Rektorys. *Variational Methods in Mathematics, Science and Engineering*. 2nd ed. Dordrecht: D. Reidel Publishing Company, 1977.
- [32] Michael A. Nielsen and Isaac L. Chuang. *Quantum Computation and Quantum Information: 10th Anniversary Edition*. Cambridge, United Kingdom: Cambridge University Press, 2010. ISBN: 978-1-107-00217-3.
- [33] Robert Beals et al. “Quantum lower bounds by polynomials”. In: *J. ACM* 48.4 (July 2001), pp. 778–797. ISSN: 0004-5411. DOI: 10.1145/502090.502097. URL: <https://doi.org/10.1145/502090.502097>.
- [34] Daan Camps et al. “Explicit Quantum Circuits for Block Encodings of Certain Sparse Matrices”. In: *SIAM Journal on Matrix Analysis and Applications* 45.1 (Mar. 2024). DOI: 10.1137/22m1484298.
- [35] Jeff S. Lundeen et al. “Direct measurement of the quantum wavefunction”. In: *Nature* 474.7350 (2011), pp. 188–191. DOI: 10.1038/nature10120. URL: <https://doi.org/10.1038/nature10120>.
- [36] Eliot Bolduc, Genevieve Gariépy, and Jonathan Leach. “Direct measurement of large-scale quantum states via expectation values of non-Hermitian matrices”. In: *Nature Communications* 7.1 (2016), p. 10439. DOI: 10.1038/ncomms10439. URL: <https://doi.org/10.1038/ncomms10439>.
- [37] Debora Ramacciotti, Andreea I. Lefterovici, and Antonio F. Rotundo. “Simple quantum algorithm to efficiently prepare sparse states”. In: *Phys. Rev. A* 110 (3 Sept. 2024), p. 032609. DOI: 10.1103/PhysRevA.110.032609. URL: <https://link.aps.org/doi/10.1103/PhysRevA.110.032609>.
- [38] Oliver O’Brien and Christoph Sünderhauf. “Quantum state preparation via piecewise QSVT”. In: *Quantum* 9 (July 2025), p. 1786. ISSN: 2521-327X. DOI: 10.22331/q-2025-07-03-1786. URL: <https://doi.org/10.22331/q-2025-07-03-1786>.
- [39] Maria Schuld et al. “Evaluating analytic gradients on quantum hardware”. In: *Phys. Rev. A* 99 (3 Mar. 2019), p. 032331. DOI: 10.1103/PhysRevA.99.032331. URL: <https://link.aps.org/doi/10.1103/PhysRevA.99.032331>.
- [40] R. Fletcher. “A new approach to variable metric algorithms”. In: *The Computer Journal* 13.3 (1970), pp. 317–322.
- [41] J. Nocedal and S. J. Wright. *Numerical Optimization*. 2nd ed. Springer, 2006.